The Astrophysical Journal, 900:115 (14pp), 2020 September 10 https://doi.org/10.3847/1538-4357/abad30

Spectral Anisotropy in 2D plus Slab Magnetohydrodynamic Turbulence in the Solar Wind and Upper Corona

G. P. Zank[1,2], M. Nakanotani[1], L.-L. Zhao[1], L. Adhikari[1], and D. Telloni[3]
[1] Center for Space Plasma and Aeronomic Research (CSPAR), University of Alabama in Huntsville, Huntsville, AL 35805, USA
[2] Department of Space Science, University of Alabama in Huntsville, Huntsville, AL 35899, USA
[3] National Institute for Astrophysics-Astrophysical Observatory of Torino Via Osservatorio 20, I-10025 Pino Torinese, Italy
Received 2020 May 12; revised 2020 July 10; accepted 2020 August 5; published 2020 September 8

Abstract

The 2D + slab superposition model of solar wind turbulence has its theoretical foundations in nearly incompressible magnetohydrodynamics (NI MHD) in the plasma beta ~ 1 or $\ll 1$ regimes. Solar wind turbulence measurements show that turbulence in the inertial range is anisotropic, for which the superposition model offers a plausible explanation. We provide a detailed theoretical analysis of the spectral characteristics of the Elsässer variables in the 2D + NI/slab model. We find that (1) the majority 2D component has a power spectrum $G^{\infty}(k_{\perp}) \sim k_{\perp}^{-5/3}$ in perpendicular wavenumber $k_{\perp}$; (2) the strongly imbalanced minority NI/slab turbulence has power spectra $G^{*}(k_{\perp}) \sim k_{\perp}^{-5/3}$ and $G^{*}(k_z) \sim k_z^{-5/3}$, where k_z is aligned with the mean magnetic field; (3) NI/slab turbulence can exhibit a double-power-law spectrum, with the steeper part being $G^{*}(k) \sim k^{-5/3}$ and corresponding to strong turbulence and the flatter spectrum satisfying $G^{*}(k) \sim k^{-3/2}$ and corresponding to weak turbulence; (4) there is a critical balance regime for NI/slab turbulence that satisfies $G^{*}(k_z) \sim k_z^{-2}$ and $G^{*}(k_{\perp}) \sim k_{\perp}^{-5/3}$; and (5) the forward and backward Elsässer power spectra can have different spectral forms provided that the triple-correlation times for each are different. We use the spectral analysis to compute the total power spectra in frequency parallel to the solar wind flow for the superposition model, showing that strongly imbalanced turbulence yields an $f^{-5/3}$ spectrum for all angles between the mean flow and magnetic field, and that double power laws are possible when the nonlinear and Alfvén timescales are both finite.

Unified Astronomy Thesaurus concepts: Interplanetary turbulence (830)

1. Introduction

Solar wind flows that are highly aligned with the mean magnetic field have been examined carefully in an attempt to identify the underlying anisotropy of low-frequency magnetohydrodynamic (MHD) turbulence (Horbury et al. 2008, 2012; Podesta 2009; Wicks et al. 2010; Forman et al. 2011; Wang et al. 2015; Telloni et al. 2019; Wu et al. 2020). Much of this work was motivated by prior studies that investigated the separation of solar wind fluctuations into slab and 2D components (Matthaeus et al. 1990; Bieber et al. 1996; Saur & Bieber 1999; Dasso et al. 2005) and its wide application to numerous solar wind problems, ranging from coronal heating (Zank et al. 2018b), to turbulence transport throughout the solar wind (Adhikari et al. 2017a), to cosmic-ray transport (Zhao et al. 2017). As summarized in Forman et al. (2011), the analyses of solar wind turbulence measurements show that turbulence in the inertial range is anisotropic, and two theoretical approaches offer plausible explanations for the observed anisotropy. These are the so-called "2D + slab" turbulence model (Matthaeus et al. 1990; Zank & Matthaeus 1992, 1993; Bieber et al. 1996) and the "critical balance" (CB) model (Goldreich & Sridhar 1995, 1997). Forman et al. (2011) fit a 2D + slab and a CB model to two sets of Ulysses data (their Figures 2 and 4) and find that both models fit the data quite well. Indeed, their Figure 4 suggests that there is little to choose between the two models. However, Forman et al. (2011) suggest that the 2D + slab model does not predict the anisotropy in power or spectrum from physical principles. This was correct at their time of writing. The theoretical foundation on which the 2D + slab or "superposition" model is based is nearly incompressible MHD (NI MHD) in the plasma beta ~ 1 or $\ll 1$ regimes (Zank & Matthaeus 1992, 1993; Hunana & Zank 2010), but until recently (Zank et al. 2017) no corresponding spectral analysis was formulated. We stress that the NI MHD decomposition in the plasma beta ~ 1 or $\ll 1$ regimes is not strictly into a 2D plus slab component—instead, the NI MHD approach separates the leading-order or dominant fluctuating component into 2D fluctuations and NI compressible corrections that include both slab (counterpropagating Alfvén waves) and higher-order quasi-2D fluctuations. This addresses in part the general criticism (e.g., Oughton & Matthaeus 2020) of the standard 2D + slab model (e.g., Bieber et al. 1996) that spectral power resides only in the 2D plane perpendicular to and along the $\hat{z}$-axis parallel to the mean magnetic field $\boldsymbol{B}_0$. The purpose of this paper is to provide a detailed spectral analysis of MHD turbulence in the solar wind from the perspective of the NI MHD form of the "2D + slab" equations, which we refer to as the 2D + NI/slab model.

Telloni et al. (2019) used Wind spacecraft data to identify 17 highly magnetic-field-aligned high-speed solar wind flows exhibiting low magnetic field compressibility. By using a Hilbert spectral analysis of arbitrary order with empirical mode decomposition, Telloni et al. (2019) were able to eliminate the effects of spurious harmonics and artifacts near sharp data transitions that plague analyses based on traditional Fourier or wavelet transforms (Huang et al. 1998). Telloni et al. (2019) find that (i) a $k_{\parallel}^{-5/3}$ magnetic field spectrum is observed persistently in the fast solar wind during periods of strong turbulence ($k_{\parallel}$ is the wavenumber parallel to the radial solar wind flow and almost parallel to the mean magnetic field) and (ii) the normalized cross-helicity is measured to be $|\sigma_c| \simeq 1$, indicative of unidirectionally propagating Alfvén waves. Both

points (i) and (ii) are inconsistent with critical balance, which generally assumes $\sigma_c \simeq 0$ (i.e., balanced turbulence with equal energy in counterpropagating Alfvén waves) and that the parallel spectrum satisfies $k_\parallel^{-2}$. Indeed, $|\sigma_c| \simeq 1$ ensures the absence of nonlinear interactions between Alfvén waves. Zhao et al. (2020a) identify examples of highly magnetic-field-aligned flow observed by the Parker Solar Probe (PSP) spacecraft, for which the magnetic power spectrum is $k_\parallel^{-5/3}$ and $|\sigma_c| \simeq 1$.

The paper is structured as follows. In Section 2, we review briefly the measurement of anisotropic spectra in the solar wind using the approach of Bieber et al. (1996) and Saur & Bieber (1999) before analyzing (Section 3) the spectral characteristics of 2D + slab models from the NI MHD perspective. Finally, conclusions are listed in Section 4.

2. Measurement of Anisotropic Spectra in the Solar Wind

Bieber et al. (1996) developed a straightforward method to use the frequency power spectra of the time series of magnetic fluctuations measured by single spacecraft in the solar wind to determine the geometry of solar wind turbulence. This approach has been adopted in numerous subsequent studies (e.g., Saur & Bieber 1999; Horbury et al. 2008; Forman et al. 2011). Since these results are needed for the theoretical modeling below, we review briefly the salient aspects of the Bieber et al. (1996) and Saur & Bieber (1999) approach and provide a modest generalization.

Let the local mean magnetic field $\boldsymbol{B}_0$ define the $\hat{\boldsymbol{z}}$-axis, and let the $\hat{\boldsymbol{x}}$-axis be defined by the plane made by the mean magnetic field and the solar wind flow velocity vector $\boldsymbol{U}_0$. The angle Ψ is the angle between $\boldsymbol{B}_0$ and $\boldsymbol{U}_0$. The $\hat{\boldsymbol{y}}$-axis is orthogonal to the $\hat{\boldsymbol{x}}$-$\hat{\boldsymbol{z}}$ plane.

For fluctuations expressed in terms of the Elsässer variables $\boldsymbol{z}^\pm = \boldsymbol{u} \pm \boldsymbol{b}/\sqrt{\mu_0 \rho_0}$, where $\boldsymbol{u}$ and $\boldsymbol{b}$ are velocity and magnetic field fluctuations about the mean fields $\boldsymbol{B}_0$ and $\boldsymbol{U}_0$ (i.e., $\boldsymbol{U} = \boldsymbol{U}_0 + \boldsymbol{u}$, $\langle \boldsymbol{U} \rangle = \boldsymbol{U}_0$, $\langle \boldsymbol{u} \rangle = 0$; $\boldsymbol{B} = \boldsymbol{B}_0 + \boldsymbol{b}$, $\langle \boldsymbol{B} \rangle = \boldsymbol{B}_0$, $\langle \boldsymbol{b} \rangle = 0$), the power spectrum associated with the two-point correlation tensor $R_{ij}^\pm(\boldsymbol{r}) = \langle z_i^\pm(\boldsymbol{x}) z_j^\pm(\boldsymbol{x}+\boldsymbol{r}) \rangle$ for spatially homogeneous turbulence can be expressed as (e.g., Zank 2014)

$$P_{ij}^\pm(\boldsymbol{k}) = \frac{1}{(2\pi)^3} \int R_{ij}^\pm e^{-i\boldsymbol{k}\cdot\boldsymbol{r}} d^3r, \tag{1}$$

for wavenumber $\boldsymbol{k}$ and separation distance $\boldsymbol{r}$. Use of the Taylor hypothesis[4] allows one to relate the temporal and spatial two-point correlation tensors using

$$R_{ij}^{\pm(t)}(t) = R_{ij}^{\pm(\boldsymbol{x})}(-U_0 \sin\Psi t,\, 0,\, -U_0 \cos\Psi t), \tag{2}$$

from which one relates the measured frequency f spectrum $P_{ij}^\pm(f)$ to the 3D wavenumber spectrum $P_{ij}^\pm(\boldsymbol{k})$,

$$P_{ij}^\pm(f) = \int e^{i2\pi f t} P_{ij}^\pm(\boldsymbol{k}) e^{-i(k_x U_0 \sin\Psi + k_z U_0 \cos\Psi)t} dt d^3k. \tag{3}$$

For turbulence axisymmetric with respect to the mean magnetic field, we will consider below either fluctuations with wavevectors aligned only with $\hat{\boldsymbol{z}}$ ($\|\boldsymbol{B}_0$), i.e., slab turbulence, or fluctuations with wavevectors only orthogonal to $\boldsymbol{B}_0$, i.e., 2D turbulence. The general form of the slab and 2D power spectral tensors is (Matthaeus & Smith 1981)

$$\text{slab:} \quad P_{xx}^{*\pm}(\boldsymbol{k}) = P_{yy}^{*\pm}(\boldsymbol{k}) = G^{*\pm}(k_z)\delta(k_x)\delta(k_y);\quad P_{zz}^{*}(\boldsymbol{k}) = 0; \tag{4}$$

$$\text{2D:} \quad P_{xx}^{\infty\pm}(\boldsymbol{k}) = \frac{G^{\infty\pm}(k_\perp)}{k_\perp^3} k_y^2 \delta(k_z);\quad P_{yy}^{\infty\pm}(\boldsymbol{k}) = \frac{G^{\infty\pm}(k_\perp)}{k_\perp^3} k_x^2 \delta(k_z);\quad P_{zz}^{\infty}(k_\perp) = 0, \tag{5}$$

where $k_\perp = \sqrt{k_x^2 + k_y^2}$, $G^*(k_z)$, and $G^\infty(k_\perp)$ are the amplitudes of slab and 2D turbulence and functions of k_z and $k_\perp$, respectively, and $\delta(x)$ is the Dirac delta function. From Equations (4) and (5), it is straightforward to show that the frequency spectra are given by (Bieber et al. 1996; Saur & Bieber 1999)

$$\text{slab:} \quad P_{xx}^{*\pm}(f) = P_{yy}^{*\pm}(f) = \frac{2\pi}{U_0 \cos\Psi} G^{*\pm}(k_z);\quad k_z = \frac{2\pi f}{U_0 \cos\Psi}; \tag{6}$$

$$\text{2D:} \quad P_{xx}^{\infty\pm}(f) = \frac{4\pi}{U_0 \sin\Psi} \int_{|k_x|}^\infty \frac{G^{\infty\pm}(k_\perp)}{k_\perp^2} \sqrt{k_\perp^2 - k_x^2}\, dk_\perp;\quad P_{yy}^{\infty\pm}(f) = \frac{4\pi}{U_0 \sin\Psi} k_x^2 \int_{|k_x|}^\infty \frac{G^{\infty\pm}(k_\perp)}{k_\perp^2} \frac{1}{\sqrt{k_\perp^2 - k_x^2}} dk_\perp;\quad k_x = \frac{2\pi f}{U_0 \sin\Psi}, \tag{7}$$

and that $P_{xx}^{\infty\pm}(f)$ and $P_{yy}^{\infty\pm}(f)$ are related through

$$P_{yy}^{\infty\pm}(f) = -f \frac{dP_{xx}^{\infty\pm}(f)}{df}. \tag{8}$$

An observed power spectrum is a superposition of both components; thus,

$$P_{\text{total}}^\pm(f) = P_{xx}^\pm(f) + P_{yy}^\pm(f). \tag{9}$$

It is typically assumed (Bieber et al. 1996; Saur & Bieber 1999; Horbury et al. 2008; Forman et al. 2011) that $G^*(k_z)$ is a power law in k_z, and similarly the integrals in Equation (7) are taken to be power laws in $k_\perp$. As we show below, the NI/slab spectrum may not be a simple power law, whereas we show that the 2D spectrum is a power law in $k_\perp$. For the slab component, if

$$P_{\text{total}}^{*\pm} = P_{xx}^{*\pm}(f) + P_{yy}^{*\pm}(f) = C^{*\pm} \frac{2\pi}{U_0 \cos\Psi} G^{*\pm}(f),$$

we have

$$P_{xx}^{*\pm}(f) = P_\parallel^{*\pm}(f) = \frac{C^{*\pm}}{2} \frac{2\pi}{U_0 \cos\Psi} G^{*\pm}(f);\quad P_{yy}^{*\pm}(f) = P_\perp^{*\pm}(f) = \frac{C^{*\pm}}{2} \frac{2\pi}{U_0 \cos\Psi} G^{*\pm}(f), \tag{10}$$

where $C^{*\pm}$ is the amplitude of the total forward/backward slab Elsässer fluctuations. For a simple power law with index $-q^*$ (i.e., $\sim k_z^{-q*}$), $G^*(f)$ would be replaced by $(2\pi/(U_0 \cos\Psi))^{q^*}$. In Equation (10), the subscripts $\parallel$ and $\perp$ refer to the Elsässer spectrum projected parallel or perpendicular to the solar wind flow vector. Similarly, for the 2D component of turbulence,

[4] This argument will need modification for observations made deep in the solar corona, where the PSP speed can no longer be neglected.

now assuming a power-law spectrum with spectral index q^∞ (i.e., $\sim k_\perp^{-q^\infty}$) (Bieber et al. 1996),

$$P_\parallel^{\infty\pm}(f) = P_{xx}^{\infty\pm}(f) = \frac{C^{\infty\pm}}{1+q^\infty}\frac{2\pi}{U_0\sin\Psi}\left(\frac{2\pi f}{U_0\sin\Psi}\right)^{-q^\infty};$$
$$P_\perp^{\infty\pm}(f) = P_{yy}^{\infty\pm}(f) = \frac{q^\infty}{1+q^\infty}C^{\infty\pm}\frac{2\pi}{U_0\sin\Psi}\left(\frac{2\pi f}{U_0\sin\Psi}\right)^{-q^\infty}, \quad (11)$$

where $C^{\infty\pm}$ is the amplitude of the total forward/backward 2D Elsässer fluctuations. Hence, for a superposition of 2D and slab fluctuations the frequency spectrum observed parallel and perpendicular to the solar wind flow is (Bieber et al. 1996; Saur & Bieber 1999; Horbury et al. 2008; Forman et al. 2011)

$$P_\parallel^{\text{total}\pm}(f) = P_\parallel^{\infty\pm}(f) + P_\parallel^{*\pm}(f) = \frac{C^{\infty\pm}}{1+q^\infty}\left(\frac{U_0\sin\Psi}{2\pi}\right)^{q^\infty-1} f^{-q^\infty} + \frac{C^{*\pm}}{2}\frac{2\pi}{U_0\cos\Psi}G^{*\pm}(f); \quad (12)$$

$$P_\perp^{\text{total}\pm}(f) = P_\perp^{\infty\pm}(f) + P_\perp^{*\pm}(f) = \frac{q^\infty}{1+q^\infty}C^{\infty\pm}\left(\frac{U_0\sin\Psi}{2\pi}\right)^{q^\infty-1} f^{-q^\infty} + \frac{C^{*\pm}}{2}\frac{2\pi}{U_0\cos\Psi}G^{*\pm}(f). \quad (13)$$

These expressions are used below. Expressions for 2D and NI/slab turbulence spectra are derived below.

3. NI MHD and 2D + Slab Models

NI MHD is a formulation of MHD in a weakly compressible or nearly incompressible regime and was developed for both homogeneous flows (Klainerman & Majda 1982; Montgomery et al. 1987; Matthaeus & Brown 1988; Zank & Matthaeus 1992, 1993) and inhomogeneous flows (Bhattacharjee et al. 1998; Hunana & Zank 2010). The solar wind and solar corona, at least away from the heliospheric current sheet, are typically in a plasma beta regime $\beta_p \sim 1$ or $\ll 1$, where $\beta_p = P/(B^2/2\mu_0)$ ($P \equiv$ thermal pressure, $B = |\boldsymbol{B}|$, $\boldsymbol{B}$ is the magnetic field, and μ_0 is the magnetic permeability). Zank & Matthaeus (1992, 1993) showed that the $\beta_p \ll 1, \sim 1$ NI MHD description comprised a superposition of a dominant 2D component (i.e., transverse magnetic fluctuations $(B_x, B_y, 0)$ in a plane orthogonal to the mean magnetic field $\boldsymbol{B}_0 = B_0\hat{\boldsymbol{z}}$ with nonzero wavenumber vector $\boldsymbol{k}_\perp = (k_x, k_y, 0)$) and a minority NI component that includes Alfvén waves with transverse fluctuations and a wavevector $k_z \| \boldsymbol{B}_0$, higher-order quasi-2D fluctuations with wavenumber vector $\boldsymbol{k}_\perp = (k_x, k_y, 0)$, and compressible fluctuations such as magnetosonic modes. Specifically, the magnetic field can be expressed as

$$\boldsymbol{B} = \boldsymbol{B}_0 + \boldsymbol{B}^\infty + \boldsymbol{B}^*, \quad (14)$$

where the NI MHD convention is that $\boldsymbol{B}^\infty$ denotes the majority 2D component of the magnetic field fluctuations and $\boldsymbol{B}^*$ describes higher-order corrections including slab, quasi-2D, and compressible fluctuations. Zank & Matthaeus (1992, 1993; see in particular the discussion about renormalization in Zank et al. 2017) showed that the ordering of the magnetic field components satisfies $|\boldsymbol{B}_0| : |\boldsymbol{B}^\infty| : |\boldsymbol{B}^*| = 1 : M_A^t : {M_A^t}^2$, where $M_A^t \equiv \langle u^2\rangle^{1/2}/V_{A0}$ denotes the turbulent Alfvén Mach number since $\langle u^2\rangle^{1/2}$ is the standard deviation of the turbulent velocity fluctuations and $V_{A0} = \sqrt{B_0^2/(\mu_0\rho_0)}$ is the mean Alfvén speed, with ρ_0 the mean background density. Since $\langle u^2\rangle^{1/2} \sim 10$ km s^{-1} and $V_{A0} \sim 50$ km s^{-1} in the solar wind, $M_A^t \sim 0.2$, which implies that $|\boldsymbol{B}^*|/|\boldsymbol{B}^\infty| \sim 0.2$, giving roughly the ratio $|\boldsymbol{B}^\infty| : |\boldsymbol{B}^*| = 80 : 20$. Rather surprisingly, given the crudeness of this estimate, Bieber et al. (1996) and Saur & Bieber (1999) find observational support in the solar wind for such a ratio of majority 2D to slab turbulence (see also Adhikari et al. 2017b; Zhao et al. 2018).

By restricting our attention to incompressible fluctuations exclusively (i.e., setting $\nabla \cdot \boldsymbol{u}^* = 0$, where $\boldsymbol{u}^*$ is the NI velocity; see Zank et al. 2017), Zank et al. (2017) introduce the "2D" (superscript "∞") and "slab"[5] (superscript "*") Elsässer variables

$$\boldsymbol{z}^{\infty\pm}(\boldsymbol{x}_\perp, t) = \boldsymbol{u}^\infty \pm \boldsymbol{B}^\infty/\sqrt{\mu_0\rho_0},$$
$$\boldsymbol{z}^{*\pm}(\boldsymbol{x}, t) = \boldsymbol{u}^* \pm \boldsymbol{B}^*/\sqrt{\mu_0\rho_0}, \quad (15)$$

to express the majority 2D and minority NI/slab NI MHD equations, respectively, as

$$\frac{\partial \boldsymbol{z}^{\infty\pm}}{\partial t} + \boldsymbol{z}^{\infty\mp}\cdot\nabla_\perp\boldsymbol{z}^{\infty\pm} = -\frac{1}{\rho_0}\nabla_\perp\left(P^\infty + \frac{B^{\infty 2}}{2\mu_0}\right);$$
$$\nabla_\perp \cdot \boldsymbol{z}^{\infty\pm} = 0; \quad (16)$$

$$\frac{\partial \boldsymbol{z}^{*\pm}}{\partial t} \mp \boldsymbol{V}_{A0}\cdot\nabla\boldsymbol{z}^{*\pm} + \boldsymbol{z}^{\infty\mp}\cdot\nabla\boldsymbol{z}^{*\pm} + \boldsymbol{z}^{*\mp}\cdot\nabla\boldsymbol{z}^{\infty\pm} + \boldsymbol{z}^{*\mp}\cdot\nabla\boldsymbol{z}^{*\pm} = -\frac{1}{\rho_0}\nabla\left(P^* + \frac{1}{\mu_0}\boldsymbol{B}_0\cdot\boldsymbol{B}^* + \frac{1}{\mu_0}\boldsymbol{B}^\infty\cdot\boldsymbol{B}^*\right);$$
$$\nabla\cdot\boldsymbol{z}^{*\pm} = 0. \quad (17)$$

Here $\boldsymbol{u}^\infty = \boldsymbol{u}^\infty(\boldsymbol{x}_\perp, t)$ and $\boldsymbol{B}^\infty = \boldsymbol{B}^\infty(\boldsymbol{x}_\perp, t)$ are the 2D velocity and magnetic field components and functions of $\boldsymbol{x}_\perp = (x, y, 0)$ only ($\hat{\boldsymbol{z}}$ is in the direction of $\boldsymbol{B}_0$), and $\nabla_\perp = (\partial_x, \partial_y)$; $\boldsymbol{u}^* = \boldsymbol{u}^*(\boldsymbol{x}, t)$ and $\boldsymbol{B}^* = \boldsymbol{B}^*(\boldsymbol{x}, t)$ are the corresponding NI/slab quantities and functions of $\boldsymbol{x} = (x, y, z)$. Equation (17) supports both Alfvén wave propagation and higher-order quasi-2D corrections to the majority 2D component. The linear wave characteristics of Equation (17) are discussed in Zank et al. (2017) (see also Zank et al. 2019).

It is important to recall (Zank & Matthaeus 1993) that Equation (16), the leading-order NI MHD description, enters at $O(M_{A0}^t)$, and the correction (17) enters at the next order $O((M_{A0}^t)^2)$, in accord with the discussion of the ordering of the magnetic field fluctuations above. Consequently, the ratio of the 2D and NI/slab energy densities is ordered as $\langle z^{*2}\rangle/\langle z^{\infty 2}\rangle \sim O((M_{A0}^t)^2)$. This ordering has to be borne in mind when developing a spectral theory of NI MHD, including

[5] We sometimes use the term "slab" somewhat loosely in the context of the NI MHD equations since the NI contribution contains both Alfvénic and higher-order (compared to the dominant "∞" contribution) quasi-2D fluctuations—a more precise statement is NI/slab fluctuations.

when comparing timescales between Equations (16) and (17). This is discussed further below.

Although the spectral analysis of the 2D incompressible Equations (16) is conventional (see Zhou et al. 2004 for an excellent discussion), some elaboration is useful for the subsequent analysis of Equation (17). The nonlinear term in Equation (16) may be approximated as

$$\boldsymbol{NL}^{\infty\pm} = \boldsymbol{z}^{\infty\pm}\frac{\langle z^{\infty\mp 2}\rangle^{1/2}}{\lambda_\perp^{\pm}} \equiv \frac{\boldsymbol{z}^{\infty\pm}}{\tau_\infty^{\pm}} \tag{18}$$

(Pouquet et al. 1976; Dobrowolny et al. 1980a, 1980b; Grappin et al. 1982, 1983; Matthaeus & Zhou 1989; Zank et al. 2012, 2017). The length scale $\lambda_\perp^{\pm}$ is the correlation length for 2D "forward" and "backward" modes, and hence $\tau_\infty^{\pm}$ is the corresponding nonlinear timescale. The ensemble-averaged one-point energy-containing transport equation for the total energy $\langle z^{\infty 2}\rangle = \langle z^{\infty +2}\rangle + \langle z^{\infty -2}\rangle$ is then simply (von Karman & Howarth 1938; Matthaeus et al. 1994; Zank et al. 1996, 2012, 2017)

$$\frac{d\langle z^{\infty 2}\rangle}{dt} = -\frac{\langle z^{\infty 2}\rangle^{3/2}}{\lambda_\perp^{\infty}}, \tag{19}$$

where we have assumed that $(\tau_\infty^{+})^{-1} = (\tau_\infty^{-})^{-1} = \langle z^{\infty 2}\rangle^{1/2}/\lambda_\perp^{\infty} = \tau_\infty^{-1}$.

Spectral transfer in the inertial range is governed by a phenomenological expression for the steady energy flux or transfer rate (Zhou et al. 2004)

$$\varepsilon = \frac{\langle z^2\rangle}{\tau_s} = \frac{\tau_3\langle z^2\rangle}{\tau_{nl}^2}, \tag{20}$$

where the spectral transfer time $\tau_s = \tau_{nl}^2/\tau_3$, τ_{nl} is the nonlinear dynamical timescale, and τ_3 is the timescale for decay of the transfer function correlations, i.e., the triple-correlation timescale.

For the 2D model Equations (16), Equations (18) and (19) show that $\tau_3 = \tau_{nl} = \lambda_\perp^{\infty}/\langle z^{\infty 2}\rangle^{1/2}$. If we assume isotropic turbulence in the 2D plane orthogonal to $\boldsymbol{B}_0$, we have

$$\left\langle z^{\infty 2}\right\rangle = \frac{1}{2\pi}\int E^{\infty}(k_\perp)d\boldsymbol{k}_\perp \sim E^{\infty}(k_\perp)k_\perp^2, \tag{21}$$

where $k_\perp = |\boldsymbol{k}_\perp|$ is the length of the wavenumber in the 2D plane and $E(k_\perp)$ is the 1D Elsässer energy spectrum, i.e., the energy between wavenumbers $k_\perp$ and $(k_\perp + dk_\perp)$ per wavenumber interval $dk_\perp$. Hence, using Equation (20), we obtain the familiar results

$$\begin{aligned}\langle z^{\infty 2}\rangle &\sim C_K\varepsilon_\infty^{2/3}k_\perp^{-2/3} \quad \text{and}\\ G^{\infty}(k_\perp) \equiv E^{\infty}(k_\perp)k_\perp &= C_K\varepsilon_\infty^{2/3}k_\perp^{-5/3},\end{aligned} \tag{22}$$

where ε_∞ is the dissipation rate of 2D incompressible MHD turbulence and C_K is the Kolmogorov constant. The majority 2D component therefore possesses the classical Kolmogorov spectrum $k_\perp^{-5/3}$ in perpendicular wavenumber.

Following Zank et al. (2017), we introduce the total NI energy $\langle z^{*2}\rangle = \langle z^{*+2}\rangle + \langle z^{*-2}\rangle$. Quite generally, we may express

$$\begin{aligned}\langle z^{*2}\rangle &= \frac{1}{2\pi}\int E^{*}(\boldsymbol{k})d\boldsymbol{k} = \frac{1}{2\pi}\int\int\int E^{*}(\boldsymbol{k}_\perp, k_z)d\boldsymbol{k}_\perp dk_z\\ &= \int\int E^{*}(k_\perp, k_z)k_\perp dk_\perp dk_z \sim E^{*}(k_\perp, k_z)k_\perp^2 k_z,\end{aligned} \tag{23}$$

after assuming isotropy in the 2D plane perpendicular to $\boldsymbol{B}_0$. Of particular importance in Equation (17) is the nonlinear interaction of the 2D ($\boldsymbol{z}^{\infty\pm}$) and NI/slab ($\boldsymbol{z}^{*\pm}$) components. Equation (17) describing the minority NI component in the incompressible limit incorporates both Alfvénic fluctuations (properly described as the slab component) and higher-order quasi-2D fluctuations. Both the slab/Alfvénic and higher-order quasi-2D fluctuations interact with the majority 2D component via passive scalar-like terms. Equation (17) includes the higher-order nonlinear term $\boldsymbol{z}^{*\mp}\cdot\nabla\boldsymbol{z}^{*\pm}$. Zank et al. (2017) included this term as an $O(M_A^{t\,4})$ correction (the remaining terms in Equation (17) are $O(M_A^{t\,2})$; see Zank & Matthaeus 1993) to derive the "richest" evolution equation.

The interaction of the NI/slab modes with the dominant 2D fluctuations is essentially a passive scalar process. This is seen as follows. From Equation (17), we can derive the one-point moment equations,

$$\begin{aligned}\frac{\partial}{\partial t}\langle z^{*\pm 2}\rangle \mp \boldsymbol{V}_{A0}\cdot\nabla\langle z^{*\pm 2}\rangle \simeq &-\frac{\langle z^{\infty 2}\rangle^{1/2}\langle z^{*\pm 2}\rangle}{\lambda_\perp^{\infty}}\\ &-\frac{\langle z^{*\mp 2}\rangle^{1/2}\langle z^{*\pm 2}\rangle}{\lambda_\perp^{*}} - \frac{\langle z^{*\mp 2}\rangle^{1/2}\langle z^{*\pm 2}\rangle^{1/2}\langle z^{\infty 2}\rangle^{1/2}}{\lambda_\perp^{*}},\end{aligned} \tag{24}$$

after crudely approximating $\langle \boldsymbol{z}^{*\pm}\cdot(\boldsymbol{z}^{*\mp}\cdot\nabla\boldsymbol{z}^{\infty\pm})\rangle$ by the last term in Equation (24) (see Zank et al. 2017 for further discussion) and assuming $\langle z^{\infty +2}\rangle = \langle z^{\infty -2}\rangle \equiv \langle z^{\infty 2}\rangle$. The inverse timescales satisfy $\langle z^{*\mp 2}\rangle^{1/2}/\lambda_\perp^{*} \ll \langle z^{\infty 2}\rangle^{1/2}/\lambda_\perp^{\infty}$ thanks to the NI ordering, and so the middle term on the right-hand side of Equation (24) is not as important as the other two. This implies that the spectral transfer associated with NI/slab fluctuations is determined by the passive coupling of $\boldsymbol{z}^{*\pm}$ fluctuations to the dominant and independently evolving $\boldsymbol{z}^{\infty\pm}$ fluctuations. On adding the two equations of Equation (24), we obtain

$$\begin{aligned}\frac{\partial}{\partial t}\langle z^{*2}\rangle - \boldsymbol{V}_{A0}\cdot\nabla E_c^{*} = &-\frac{\langle z^{\infty 2}\rangle^{1/2}\langle z^{*2}\rangle}{\lambda_\perp^{\infty}}\\ &-2\frac{\langle z^{*-2}\rangle^{1/2}\langle z^{*+2}\rangle^{1/2}\langle z^{\infty 2}\rangle^{1/2}}{\lambda_\perp^{*}},\end{aligned} \tag{25}$$

where $E_c^{*} \equiv \langle z^{*+2}\rangle - \langle z^{*-2}\rangle$ is the NI/slab cross-helicity (the normalized NI/slab cross-helicity is given by $\sigma_c^{*} \equiv E_c^{*}/\langle z^{*2}\rangle$). For fully balanced turbulence with $\langle z^{*+2}\rangle = \langle z^{*-2}\rangle$, $E_c^{*} = 0$ in Equation (25), which becomes

$$\frac{\partial}{\partial t}\langle z^{*2}\rangle = -\frac{\langle z^{\infty 2}\rangle^{1/2}\langle z^{*2}\rangle}{\lambda_\perp^{\infty}} - \frac{\langle z^{\infty 2}\rangle^{1/2}\langle z^{*2}\rangle}{\lambda_\perp^{\infty}}\frac{\lambda_\perp^{\infty}}{\lambda_\perp^{*}}. \tag{26}$$

Since it is reasonable to assume that $\lambda_\perp^{\infty} \sim \lambda_\perp^{*}$, the dissipation rate ε_* is determined to within a factor of $\sim$2 from the

dominant 2D component,

$$\varepsilon_* = \langle z^{\infty 2}\rangle^{1/2} k_\perp \langle z^{*2}\rangle = C_K^{1/2}\varepsilon_\infty^{1/3} k_\perp^{2/3}\langle z^{*2}\rangle. \quad (27)$$

From Equation (23), we therefore obtain the spectrum

$$E^*(k_\perp, k_z)k_\perp^2 = C_K^{-1/2}\varepsilon_* \varepsilon_\infty^{-1/3} k_\perp^{-2/3} k_z^{-1}. \quad (28)$$

Thus, for $k_\perp = k_z$ the Kolmogorov spectrum $G^*(k_\perp) \equiv E^* k_\perp^2 \sim k_\perp^{-5/3}$ holds. This spectrum is the result of the passive coupling of $z^{*\pm}$ to the turbulent dominant 2D fluctuations and is not due to nonlinear couplings between $z^{*\pm}$ modes (the second and third terms on the right-hand side of Equation (24)). We discuss the incorporation of spectral coupling between the $z^{*\pm}$ components and the passive coupling to $z^{\infty\pm}$ below.

Consider now the opposite limit in which all the energy resides in a single NI component, say, $\langle z^{*+2}\rangle \neq 0$ and $\langle z^{*-2}\rangle = 0$. In this case, Equation (24) yields exactly

$$\frac{\partial}{\partial t}\langle z^{*+2}\rangle - \boldsymbol{V}_{A0}\cdot\nabla\langle z^{*+2}\rangle = -\frac{\langle z^{\infty 2}\rangle^{1/2}\langle z^{*+2}\rangle}{\lambda_\perp^\infty}, \quad (29)$$

and the $\langle z^{*-2}\rangle$ equation is identically zero. Unlike Equation (25), in which we neglected the higher-order nonlinear terms, the corresponding nonlinear terms are identically zero in Equation (29). If there were no passive coupling to the 2D modes, Equation (29) would describe the evolution of the energy density in unidirectionally propagating Alfvén waves. In this case, on letting ε_*^A denote the dissipation rate of $\langle z^{*+2}\rangle$, the same reasoning as above shows that Equation (28) holds (with ε_* replaced by ε_*^A) and $G^*(k_z) \sim k_z^{-5/3}$ and $G^*(k_\perp) \sim k_\perp^{-5/3}$ for $k_\perp = k_z$. Hence, the passive scalar response of unidirectionally propagating Alfvén waves to dominant 2D turbulence is a $k^{-5/3}$ spectrum.

Consider now the timescales for NI MHD. The dissipation term for the 2D Elsässer total energy density $\langle z^{\infty 2}\rangle$ is

$$\frac{\langle z^{\infty 2}\rangle^{1/2}\langle z^{\infty 2}\rangle}{\lambda_\perp^\infty} = \frac{\langle z^{\infty 2}\rangle}{\tau_\infty},$$

after defining the 2D nonlinear timescale, from Equation (16), as

$$\tau_\infty^{-1} = \frac{\langle z^{\infty 2}\rangle^{1/2}}{\lambda_\perp^\infty}. \quad (30)$$

The higher-order Alfvénic terms can be expressed dimensionally as

$$\boldsymbol{V}_{A0}\cdot\nabla\langle z^{*\pm 2}\rangle \sim \frac{V_{A0}\langle z^{*\pm 2}\rangle}{\lambda_A^\pm},$$

where the Alfvén correlation lengths $\lambda_A^\pm$ have been introduced. The ratio of the 2D and Alfvénic terms above is

$$\frac{V_{A0}}{\lambda_A^\pm}\frac{\langle z^{*\pm 2}\rangle}{\langle z^{\infty 2}\rangle}\tau_\infty \sim \frac{V_{A0}}{\lambda_A^\pm}(M_{A0}^t)^2\tau_\infty = \frac{\tau_\infty}{\tau_A},$$

after defining the NI Alfvén timescale as

$$\tau_A^{-1} = \frac{V_{A0}}{\lambda_A}(M_{A0}^t)^2. \quad (31)$$

The form of the Alfvén timescale is consistent with the NI MHD ordering explicit in the NI decomposition (16) and (17) of the MHD equations. Expression (31) is the NI MHD form of the usual Alfvén timescale V_{A0}/λ_A. Finally, the NI nonlinear timescale is of order $(M_{A0}^t)^2$ higher than the Alfvén timescale, from the same argument as above, and is given by

$$\tau_*^{-1} = \frac{\langle z^{*2}\rangle^{1/2}}{\lambda_\perp^*}(M_{A0}^t)^2, \quad (32)$$

where the higher-order NI nonlinear correlation length $\lambda_\perp^*$ has been introduced. Since $\langle z^{*2}\rangle/\langle z^{\infty 2}\rangle \sim O((M_{A0}^t)^2)$, the timescale of Equation (32) is $O((M_{A0}^t)^4)$, which is consistent with the NI ordering implicit in Equation (17) and that the nonlinear term was included as a higher-order correction to determine the richest evolution equation (Zank et al. 2017). The correlation length is the characteristic length scale for the spatial decorrelation of turbulence and is independent of wavenumber.

Before concluding this discussion, let us reconsider briefly the form of the Alfvén timescale (31). There are two properties that the Alfvén timescale should capture ideally: (1) For unidirectional Alfvén wave propagation, Equation (29) holds, i.e., the Alfvénic term is a propagation term exclusively and does not contribute to spectral transfer. (2) Spectral transfer mediated by the Alfvén term is possible only when $\langle z^{*+2}\rangle \neq \langle z^{*-2}\rangle \neq 0$, for which $E_c^* \neq 0$. These two effects are not captured by the Alfvén timescale (31). The left-hand side of Equation (25) can be rewritten as

$$\frac{\partial}{\partial t}\langle z^{*2}\rangle - \boldsymbol{V}_{A0}\cdot\nabla(\langle z^{*+2}\rangle - \langle z^{*-2}\rangle) = \frac{\partial}{\partial t}\langle z^{*2}\rangle - \boldsymbol{V}_{A0}\cdot\nabla\left(\frac{\langle z^{*+2}\rangle}{\langle z^{*2}\rangle} - \frac{\langle z^{*-2}\rangle}{\langle z^{*2}\rangle}\right)\langle z^{*2}\rangle. \quad (33)$$

Expressed in this form, Equation (33) shows that there are two timescales associated with the Alfvén term,

$$\tau_{A+}^{-1} \equiv \frac{V_{A0}}{\lambda_A^+}\frac{\langle z^{*+2}\rangle}{\langle z^{*2}\rangle}M_{A0}^{t\,2} \quad \text{and} \quad \tau_{A-}^{-1} \equiv \frac{V_{A0}}{\lambda_A^-}\frac{\langle z^{*-2}\rangle}{\langle z^{*2}\rangle}M_{A0}^{t\,2}.$$

For a single spectral transfer timescale that captures properties (1) and (2) above, we construct

$$(\tau_A^{-1})^2 \equiv (\tau_{A+}^{-1})(\tau_{A-}^{-1}) = \frac{V_{A0}^2}{\lambda_A^2}\frac{\langle z^{*+2}\rangle\langle z^{*-2}\rangle}{\langle z^{*2}\rangle^2}M_{A0}^{t\,4},$$

after setting $\lambda_A^+ = \lambda_A^- = \lambda_A$, i.e.,

$$\tau_A^{-1} = \frac{V_{A0}}{\lambda_A}\frac{\langle z^{*+2}\rangle^{1/2}\langle z^{*-2}\rangle^{1/2}}{\langle z^{*2}\rangle}M_{A0}^{t\,2} = \frac{V_{A0}}{\lambda_A}(1-\sigma_c^{*2})^{1/2}M_{A0}^{t\,2}, \quad (34)$$

since $\langle z^{*+2}\rangle\langle z^{*-2}\rangle/\langle z^{*2}\rangle = (\langle z^{*2}\rangle + E_C^*)(\langle z^{*2}\rangle - E_C^*)/\langle z^{*2}\rangle = 1 - \sigma_c^{*2}$. This simple extension of Equation (31) captures properties (1) and (2) above. We have (i) $\tau_A^{-1} = 0$ if $|\sigma_c^*| = 1$, i.e., no spectral transfer can occur for unidirectional Alfvén wave propagation (unless mediated by the "passive" response to 2D turbulence), and (ii) balanced turbulence yields $\tau_A^{-1} = (V_{A0}/\lambda_A)(M_{A0}^t)^2$ since $|\sigma_c^*| = 0$. We treat $s \equiv (1-\sigma_c^{*2})^{1/2}$, $s \in [0, 1]$, as a parameter in the analysis below.

Let us return to the full spectral interaction problem for the NI component, for which the passive scalar coupling discussed above is moderated by Alfvén wave propagation effects and the

weaker (in terms of NI orderings) nonlinear term. For slab and 2D fluctuations to interact, the Alfvén and nonlinear spectral timescales cannot be completely disparate, i.e., neither quasi-2D nor wave propagation processes should be so strong that one controls the decorrelation of the other. If quasi-2D nonlinear interactions dominate (the spectral timescale inequality $\tau_\infty(\boldsymbol{k}_\perp) \ll \tau_A(k_z)$ must hold), the turbulence may be thought of as strong, whereas if wave propagation processes dominate ($\tau_\infty(\boldsymbol{k}_\perp) \gg \tau_A(k_z)$), the turbulence is described as weak. The $\tau_A \to \infty$ limit was discussed above, and Alfvén wave propagation and 2D turbulence are fully decorrelated, responding only in a passive sense to 2D turbulence. For the present with τ_A finite, the NI fluctuations $\boldsymbol{z}^{*\pm}$ possess both slab/Alfvénic (i.e., nonzero k_z) and quasi-2D ($\boldsymbol{k}_\perp$) modes distinct from the $\boldsymbol{z}^{\infty\pm}$ fluctuations that are exclusively 2D. Nonetheless, NI interactions are dominated by their interaction with the majority 2D $\boldsymbol{z}^{\infty\pm}$ modes (in this case, the passive scalar-like resonant interaction yields $\boldsymbol{k}''' = \boldsymbol{k}' + \boldsymbol{k}''$, $\pm\ \boldsymbol{V}_{A0} \cdot \boldsymbol{k}''' = -\ \boldsymbol{V}_{A0} \cdot \boldsymbol{k}''$, where $\boldsymbol{k}'$ is the wavenumber of a zero-frequency dominant 2D $\boldsymbol{z}^{\infty\pm}$ mode, $\boldsymbol{k}''$ is the wavenumber of a $\boldsymbol{z}^{*\pm}$ mode $\propto \exp[i\boldsymbol{k}'' \cdot (\boldsymbol{x} \mp \boldsymbol{V}_{A0} t)]$, and $\boldsymbol{k}'''$ is the wavenumber of the resonantly excited $\boldsymbol{z}^{*\pm}$ mode), showing that the energy transfer occurs primarily in $\boldsymbol{k}_\perp$ as usual. Hence, energy transfer in the NI regime is not due primarily to counterpropagating slab/Alfvén fluctuations, and indeed energy transfer continues efficiently even when the normalized cross-helicity is close to ± 1.

As indicated by Equation (24) and consistent with Equations (31)–(32), the three timescales that govern spectral transfer for $\boldsymbol{z}^{*\pm}$ in the case of imbalanced and fully balanced turbulence are $\tau_A^{-1} \sim sV_{A0}(M_{A0}^t)^2 k_z$, $\tau_\infty^{-1} \sim \langle z^{\infty 2}\rangle^{1/2} k_\perp$, and $\tau_*^{-1} \sim \langle z^{*2}\rangle^{1/2} k_\perp$. These timescales can be used to form the effective triple-correlation time τ_3 (Equation (20)), which, together with the higher-order NI/slab nonlinear timescale τ_* (Equation (32)), allows us to express the spectral transfer time τ_s as $\tau_*^2 = \tau_3 \tau_s$. On following the suggestion of Matthaeus & Zhou (1989), Zhou & Matthaeus (1990), and Zhou et al. (2004), we may invoke a Kolmogorov phenomenology for the NI/slab Equation (17), i.e.,

$$\varepsilon_* = \tau_3 \frac{\langle z^{*2}\rangle}{\tau_*^2} \tag{35}$$

(ε_* is the NI/slab dissipation rate), and express the triple-correlation time τ_3 as

$$\begin{aligned}\tau_3^{-1} &= \frac{1}{\tau_\infty} + \frac{1}{\tau_A} + \frac{1}{\tau_*} \simeq \frac{1}{\tau_\infty} + \frac{1}{\tau_A} \\ &= \langle z^{\infty 2}\rangle^{1/2} k_\perp + sV_{A0} M_{A0}^{t\,2} k_z \\ &= C_K^{1/2} \varepsilon_\infty^{1/3} k_\perp^{2/3} \left(1 + \left(\frac{s^3 V_{A0}^3 (M_{A0}^t)^6}{C_K^{3/2}\varepsilon_\infty}\right)^{1/3} k_z k_\perp^{-2/3}\right).\end{aligned} \tag{36}$$

From Equation (35), using $\tau_*^{-1} = \langle z^{*2}\rangle^{1/2} k_\perp$, we find $\varepsilon_* = \tau_3 \langle z^{*2}\rangle^2 k_\perp^2$, which, from Equation (23), yields

$$\begin{aligned}E^*(k_z, k_\perp) k_\perp^2 &= \varepsilon_*^{1/2} \tau_3^{-1/2} k_\perp^{-1} k_z^{-1} = C_K^{1/4} \varepsilon_*^{1/2} \varepsilon_\infty^{1/6} k_\perp^{-2/3} k_z^{-1} \\ &\times \left(1 + \left(\frac{s^3 V_{A0}^3 (M_{A0}^t)^6}{C_K^{3/2}\varepsilon_\infty}\right)^{1/3} k_z k_\perp^{-2/3}\right)^{1/2}.\end{aligned} \tag{37}$$

For strongly imbalanced turbulence, $\tau_A \gg \tau_\infty$, and we recover Equation (28) other than some slight differences in the dissipation constants.

To examine the content of Equation (37) a little more closely, introduce a transitional wavenumber $k_t^{-1} \equiv (s^3 V_{A0}^3 (M_{A0}^t)^6 / C_K^{3/2}\varepsilon_\infty)$ and note that the ratio of the 2D nonlinear timescale τ_∞ to the Alfvén timescale τ_A is simply

$$\begin{aligned}\frac{\tau_\infty}{\tau_A} &= \left(\frac{s^3 V_{A0}^3 (M_{A0}^t)^6}{C_K^{3/2}\varepsilon_\infty}\right)^{1/3} k_z k_\perp^{-2/3} = \frac{k_\perp^{-2/3} k_z}{k_t^{1/3}} \\ &= \left(\frac{k_\perp}{k_t}\right)^{-2/3} \left(\frac{k_z}{k_t}\right).\end{aligned} \tag{38}$$

Since the 2D dissipation rate is governed by $C_K^{-3/2}\varepsilon_\infty = \langle z^{\infty 2}\rangle^{3/2}/\lambda_\perp^\infty$,

$$\begin{aligned}k_t^{-1} &= \frac{s^3 V_{A0}^3 (M_{A0}^t)^6}{C_K^{3/2}\varepsilon_\infty} = \frac{s^3 V_{A0}^3 (M_{A0}^t)^6}{\langle z^{\infty 2}\rangle^{3/2}} \lambda_\perp^\infty \\ &= s^3 \frac{(M_{A0}^t)^6}{(M_{A0}^\infty)^3} \lambda_\perp^\infty,\end{aligned} \tag{39}$$

where $M_{A0}^{\infty 2} \equiv \langle z^{\infty 2}\rangle / V_{A0}^2 = (\langle u^{\infty 2}\rangle + \langle B^{\infty 2}/\mu\rho_0\rangle)/V_{A0}^2$. Recall that the NI MHD expansion is based on $M_{A0}^t = \langle u^2\rangle^{1/2}/V_{A0} \ll 1$, whereas M_{A0}^∞ here is defined by the kinetic and magnetic energy density in fluctuations, implying $M_{A0}^\infty > M_{A0}^t$. Evidently, $k_t > (\lambda_\perp^\infty)^{-1}$, but it depends on the magnitude of M_{A0}^t and the level of imbalance in the NI/slab component (i.e., s) whether k_t falls into the inertial range of observed turbulence or not. Unidirectional wave propagation implies $s = 0$ and $k_t^{-1} = 0$. The physical content of k_t is threefold. First, it delineates wavenumber regions of strong and weak turbulence. From Equations (37) and (38), $k_\perp^{-2/3} k_z < k_t^{1/3} = M_A^\infty / (sM_{A0}^t)^2 (\lambda_\perp^\infty)^{-1/3}$ implies that $\tau_\infty < \tau_A$, and hence the turbulence in this wavenumber regime is strong and dominated by quasi-2D interactions. By contrast, $k_\perp^{-2/3} k_z > k_t^{1/3}$ implies the 2D timescale $\tau_\infty > \tau_A$, and the turbulence in this wavenumber regime is weak and dominated by propagation effects associated with Alfvén wave interactions. The wavenumber space in which these two regimes exist is illustrated in Figure 1, where the bounding curve

$$k_\perp = \frac{s^{3/2} (M_{A0}^t)^3 \lambda_\perp^\infty}{(M_{A0}^\infty)^{3/2}} k_z^{3/2} \tag{40}$$

separates the region where $\tau_\infty <$ or $> \tau_A$. Three curves corresponding to the choices of $s = 0.01$, 0.1, and 1 are shown. Figure 1 also shows that the NI/slab model includes wave power in the full wavenumber plane and not only along the mean magnetic field direction. The presence of wave power in the full wavenumber plane distinguishes the 2D + NI/slab model (Zank et al. 2017) from the standard 2D + slab model (Bieber et al. 1996; Oughton & Matthaeus 2020). Second, if plasma conditions are such that the transitional wavenumber k_t falls outside the inertial range, then the inertial range spectral index will be determined by whether the turbulence is in the strong or weak regime, i.e., $-5/3$ or $-3/2$, as observed in solar wind data. Third, as we discuss below, if k_t happens to fall into the inertial range (i.e., is smaller than the dissipation scale), it

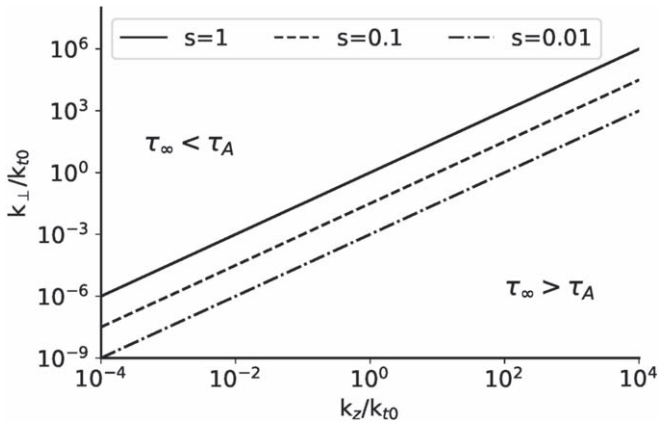

Figure 1. Plot showing the strong ($\tau_\infty < \tau_A$) and weak ($\tau_\infty > \tau_A$) turbulence regimes in NI/slab wavenumber space. The boundary curve in the figure is given by Equation (40) and corresponds to the critical balance condition $\tau_\infty = \tau_A$. Three curves corresponding to the choices of $s = 0.01$, 0.1, and 1 are shown. The normalization is to $k_{t0}^{-1} \equiv k_t^{-1}(s = 1) = (M_{A0}^t)^6/(M_{A0}^\infty)^3\lambda_\perp^\infty$. See text for details.

identifies a point at which the inertial range spectrum changes slope asymptotically.

Consider now a possible relationship between $k_\perp$ and k_z, provided that it exists, such that

$$k_\perp = \frac{k_z{}^a}{k_t^{a-1}}, \tag{41}$$

for $a > 0$ and $s \neq 0$. Evidently, from Equation (38) an arbitrary choice of a preserves dimensionality. In the context of the minority NI/slab component, the parameter a is simply a measure of wavenumber anisotropy, with $a = 1$ meaning isotropy. Wavenumber anisotropy has been discussed in terms of the velocity and magnetic field fluctuations having correlation lengths different in the direction perpendicular to the magnetic field than in the parallel direction, as suggested by the so-called "Maltese Cross" configuration of the correlation function (see Matthaeus et al. 1990; Dasso et al. 2005; Weygand et al. 2009; Ruiz et al. 2011; Horbury et al. 2012). On substituting Equation (41) into Equation (37), we obtain expressions in either k_z or $k_\perp$,

$$G^*(k_z) \equiv E^*(k_z, k_\perp)k_\perp^2 = C_K^{1/4}\varepsilon_*^{1/2}\varepsilon_\infty^{1/6}k_t^{2(a-1)/3}k_z^{-(2a+3)/3} \times \left(1 + \left(\frac{k_z}{k_t}\right)^{-(2a-3)/3}\right)^{1/2}; \tag{42}$$

$$E^*(k_z, k_\perp)k_\perp^2 = C_K^{1/4}\varepsilon_*^{1/2}\varepsilon_\infty^{1/6}k_t^{-(a-1)/a}k_\perp^{-(2a+3)/3a} \times \left(1 + \left(\frac{k_\perp}{k_t}\right)^{-(2a-3)/3a}\right)^{1/2}. \tag{43}$$

We need to be careful in interpreting Equations (42) and (43) as spectra in k_z or $k_\perp$. Consider the spectrum in $k_\perp$ first. From Equation (23)

$$\begin{aligned}\langle z^{*2}\rangle &= \int\int E^*(k_\perp, k_z)k_\perp dk_\perp dk_z \\ &\simeq \int E^*(k_\perp, k_z)k_\perp k_z dk_\perp \\ &= k_t^{(a-1)/a}\int E^*(k_\perp, k_z)k_\perp^2 k_\perp^{-(a-1)/a}dk_\perp,\end{aligned}$$

which yields, after using Equation (43),

$$\langle z^{*2}\rangle = \varepsilon_*^{1/2}\varepsilon_\infty^{1/6}\int k_\perp^{-5/3}\left(1 + \left(\frac{k_\perp}{k_t}\right)^{-(2a-3)/3a}\right)^{1/2}dk_\perp. \tag{44}$$

The 1D spectrum for $k_\perp$ is therefore given by

$$G^*(k_\perp) \equiv E^*(k_\perp)k_\perp k_z = C_K^{1/4}\varepsilon_*^{1/2}\varepsilon_\infty^{1/6}k_\perp^{-5/3} \times \left(1 + \left(\frac{k_\perp}{k_t}\right)^{-(2a-3)/3a}\right)^{1/2}, \tag{45}$$

which is always $\sim k_\perp^{-5/3}$ for $\tau_A > \tau_\infty$ regardless of the choice of a. For $\tau_A < \tau_\infty$, Equation (45) yields $\sim k_\perp^{-(4a-1)/2a}$, for which the choice of $a = 1$ then yields the perpendicular spectrum as $\sim k^{-3/2}$, i.e., the Iroshnikov–Kraichnan (IK) spectrum. This should be expected since $\tau_A < \tau_\infty$ implies that Alfvén wave propagation effects dominate.

A related argument shows that the 1D spectrum for k_z is given exactly by Equation (42).

Several points are immediately apparent about the NI/slab spectra (42) and (43). Recall that the second term under the square root is the ratio $\tau_\infty(k_z, k_\perp)/\tau_A(k_z)$. Evidently, the choice of $a = 3/2$ renders the timescale ratio τ_∞/τ_A independent of wavenumber, and one finds from Equation (42)

$$G^*(k_z) = \sqrt{2}\,\frac{\varepsilon_*^{1/2}\varepsilon_\infty^{1/2}}{V_{A0}}k_z^{-2}, \tag{46}$$

for example (Goldreich & Sridhar 1995, 1997). If $a < 3/2$, then both wavenumber regimes $k_z < k_t$ and $k_\perp < k_t$ correspond to $\tau_\infty < \tau_A$ (implying that 2D nonlinear interactions dominate), whereas the wavenumber regimes $k_t < k_z$ and $k_t < k_\perp$ are equivalent to $\tau_\infty > \tau_A$ (implying that wave-like interactions dominate larger wavenumbers). By contrast, for $a > 3/2$, these regimes are swapped, and instead both $k_z < k_t$ and $k_\perp < k_t$ correspond to $\tau_\infty > \tau_A$ (wave-dominated regime) and $k_t < k_z$ and $k_t < k_\perp$ imply $\tau_\infty < \tau_A$ (dominated by nonlinear interactions).

For strongly imbalanced turbulence $s \ll 1$, we can neglect the τ_A^{-1} term in Equation (37) to obtain the inertial range spectrum for the NI/slab turbulence component as

$$\begin{aligned}G^*(k_\perp) &= \varepsilon_*^{1/2}\varepsilon_\infty^{1/6}k_\perp^{-5/3} \quad \text{and} \\ G^*(k_z) &= \varepsilon_*^{1/2}\varepsilon_\infty^{1/6}k_t^{2(a-1)/3}k_z^{-(2a+3)/3},\end{aligned} \tag{47}$$

or $G^*(k_z) \sim k_z^{-5/3}$ if $a = 1$. Evidently this is the only choice that yields a Kolmogorov spectrum. Moreover, when $s \ll 1$ or even 0, $k_t^{-1} = 0$ and only $a = 1$ ensures that Equation (47) is sensibly defined. Of course, one can introduce an arbitrary normalization. As we discuss further below, this result, in combination with the dominant 2D component, may describe the highly magnetic field −solar wind flow-aligned observations of Telloni et al. (2019)

and Zhao et al. (2020a), i.e., strongly imbalanced Alfvén wave propagation $|\sigma_*| \simeq 1$ and a $k_\parallel^{-5/3}$ spectrum (here $\parallel$ refers to the spectrum parallel to the flow vector). This requires, however, that $a = 1$ ($k_\perp = k_z$).

Although formally allowed, the choice of $a = 3/2$ in Equation (47), which gives the spectrum for fluctuations aligned with $\boldsymbol{B}_0$ as $\sim k_z^{-2}$ (and for fluctuations perpendicular to $\boldsymbol{B}_0$ as $\sim k_\perp^{-5/3}$), is inconsistent with the critical balance assumption of $\tau_A = \tau_\infty$ (Goldreich & Sridhar 1995, 1997).

On assuming that τ_∞ and τ_A are finite, the asymptotic forms corresponding to spectra (42) and (45) are

$$a < \frac{3}{2}: \quad G^*(k_z) \sim \begin{cases} k_z^{-(2a+3)/3} & k_z < k_t \quad (\tau_\infty < \tau_A) \\ k_z^{-(2a+1)/2} & k_t < k_z \quad (\tau_\infty > \tau_A) \end{cases};$$

$$G^*(k_\perp) \sim \begin{cases} k_\perp^{-5/3} & k_\perp < k_t \quad (\tau_\infty < \tau_A) \\ k_\perp^{-(4a-1)/2a} & k_t < k_\perp \quad (\tau_\infty > \tau_A) \end{cases}; \tag{48}$$

$$a = \frac{3}{2}: \quad G^*(k_z) \sim k_z^{-2} \qquad (\tau_\infty = \tau_A);$$

$$G^*(k_\perp) \sim k_\perp^{-5/3} \qquad (\tau_\infty = \tau_A); \tag{49}$$

$$a > \frac{3}{2}: \quad G^*(k_z) \sim \begin{cases} k_z^{-(2a+1)/2} & k_z < k_t \quad (\tau_\infty > \tau_A) \\ k_z^{-(2a+3)/3} & k_t < k_z \quad (\tau_\infty < \tau_A) \end{cases};$$

$$G^*(k_\perp) \sim \begin{cases} k_\perp^{-(4a-1)/2a} & k_\perp < k_t \quad (\tau_\infty > \tau_A) \\ k_\perp^{-5/3} & k_t < k_\perp \quad (\tau_\infty < \tau_A) \end{cases}. \tag{50}$$

It is straightforward to see that the NI/slab double-power-law spectra predicted by Equation (42) and (45) and Equation (48) and (50) for both $a < 3/2$ and $a > 3/2$ possess a steeper slope for $k_z < k_t$ that then flattens for $k_t < k_z$.

As discussed above, the choice of $a = 1$ yields

$$G^*(k_z) \sim G^*(k_\perp) \sim \begin{cases} k_z^{-5/3} \sim k_\perp^{-5/3} & k_z, k_\perp < k_t \quad (\tau_\infty < \tau_A) \\ k_z^{-3/2} \sim k_\perp^{-3/2} & k_t < k_z, k_\perp \quad (\tau_\infty > \tau_A) \end{cases}, \tag{51}$$

showing that the wavenumber regime smaller than the transitional wavenumber k_t is asymptotic to the Kolmogorov spectrum and dominated by quasi-2D nonlinear interactions. The wavenumber regime for $k_z > k_t$ admits IK scaling asymptotically and is dominated by wave-like interactions. The general NI/slab spectrum for $a = 1$ is illustrated in the top row of Figure 2, showing that the $k^{-5/3} = k_z^{-5/3} = k_\perp^{-5/3}$ spectrum transitions to a $k^{-3/2}$ spectrum at $k = k_t$. Some evidence for the flattening of Elsässer spectra has been found in Helios data (Tu et al. 1989, 1990; Marsch & Tu 1990).

We note that the choice of $a = 3$ (i.e., $k_\perp = k_z^3 k_t^{-2}$) yields the spectrum

$$G^*(k_\perp) \sim \begin{cases} k_\perp^{-11/6} & (\tau_\infty > \tau_A) \\ k_\perp^{-5/3} & (\tau_\infty < \tau_A) \end{cases};$$

$$G^*(k_z) \sim \begin{cases} k_z^{-7/2} & (\tau_\infty > \tau_A) \\ k_z^{-3} & (\tau_\infty < \tau_A) \end{cases}. \tag{52}$$

Plots of the NI/slab compensated spectra are plotted in Figure 2 for $a = 1$, $3/2$, and 3, corresponding to the three cases discussed above. The wavenumber regimes in which $\tau_A \ll (\gg)\tau_\infty$ for the $a \neq 3/2$ cases are identified.

In closing this discussion, consider briefly the separate spectra of $\langle z^{*+2}\rangle$ and $\langle z^{*-2}\rangle$ (e.g., Dobrowolny et al. 1980a, 1980b; Marsch 1991; Zhou et al. 2004; Zank et al. 2012). Generalizing the above slightly, we set

$$\varepsilon_*^\pm = \frac{\langle z^{*\pm 2}\rangle}{\tau_s^\pm} = \tau_3^\pm \frac{\langle z^{*\pm 2}\rangle}{\tau_{*\mp}^2}, \tag{53}$$

where $\tau_{*\mp}^{-1} = \langle z^{*\mp 2}\rangle^{1/2} k_\perp$. This yields simply $\varepsilon_*^\pm = \tau_3^\pm \langle z^{*+2}\rangle \langle z^{*-2}\rangle k_\perp^2$, which from Equation (23) yields $\langle z^{*\pm 2}\rangle \simeq E^{*\pm} k_\perp^2 k_z$. Hence, $\varepsilon_*^\pm = \tau_3^\pm E^{*+} E^{*-} k_\perp^6 k_z^2$. There are several possibilities in choosing $\tau_3^\pm$. If we choose to use Equation (36), then $\tau_3^+ = \tau_3^-$, which implies $\varepsilon_*^+ = \varepsilon_*^-$ and $E^{*+} = E^{*-}$. In this case,

$$E^{*+}(k_\perp, k_z) k_\perp^2 = E^{*-}(k_\perp, k_z) k_\perp^2 = C_K^{1/4} \varepsilon_*^{1/2} \varepsilon_\infty^{1/6} k_\perp^{-2/3} k_z^{-1} \times \left(1 + \frac{k_z k_\perp^{-2/3}}{k_t^{1/3}}\right)^{1/2}, \tag{54}$$

from which the corresponding results for $G^{*\pm}(k_\perp)$ and $G^{*\pm}(k_z)$, Equation (42) or Equation (45), follow as before, i.e., both the G^{*+} and G^{*-} spectra are steeper for $k < k_t$ and flatter for $k > k_t$.

Alternatively, one might argue that $\tau_3^+ \neq \tau_3^-$, in which case different spectra for G^{*+} and G^{*-} would result. For example, suppose that $\tau_A \gg \tau_\infty$ for $\langle z^{*+2}\rangle$, giving $G^{*+}(k_\perp) \sim k_\perp^{-5/3}$ for $a = 1$. Conversely, if τ_A and τ_∞ are both finite for $\langle z^{*-2}\rangle$ and $a = 1$, then the spectra for $G^{*-}(k_\perp)$ and $G^{*-}(k_z)$ have the asymptotic form given by Equation (48), i.e., $G^{*-}(k_\perp) \sim k_\perp^{-5/3}$, $k_\perp < k_t$; $\sim k_\perp^{-3/2}$, $k_t < k_\perp$ and $G^{*-}(k_z) \sim k_z^{-5/3}$, $k_z < k_t$; $\sim k_z^{-3/2}$, $k_t < k_z$. Hence, G^{*+} and G^{*-} can have different spectral forms, such as found by Tu et al. (1989, 1990) and Marsch & Tu (1990)—see in particular Figure 2 of Tu et al. (1989). However, observations of the total spectrum will reflect the mediation by the dominant 2D component, which depends on the obliquity between the solar wind flow and magnetic field vectors, as discussed below.

Let us now consider the spectrum of 2D + NI/slab fluctuations measured by a spacecraft in the solar wind based on the formulation above. For this discussion, we will consider three choices of a. For the first, we take $a = 1$ for the NI/slab turbulence because asymptotically this choice yields the Kolmogorov spectrum when $\tau_A > \tau_\infty$ and the IK spectrum in the opposite regime. For the second, we choose $a = 3/2$ since it yields the critical balance spectrum in k_z and $k_\perp$ for the NI/slab component. The third case is $a = 3$. We will also consider $a = 1$ but for $\tau_A \gg \tau_\infty$, corresponding to $G^*(k_z) \sim k_z^{-5/3}$. From Sections 2 and 3, we can use

$$a = 1: \quad G^*(k_z) = C_* k_z^{-5/3} \left(1 + \left(\frac{k_z}{k_t}\right)^{1/3}\right)^{1/2}, \tag{55}$$

$$a = 1, \quad \tau_A \gg \tau_\infty: \quad G^*(k_z) = C_* k_z^{-5/3}, \tag{56}$$

$$a = \frac{3}{2}: \quad G^*(k_z) = C_* k_t^{1/3} k_z^{-2}, \tag{57}$$

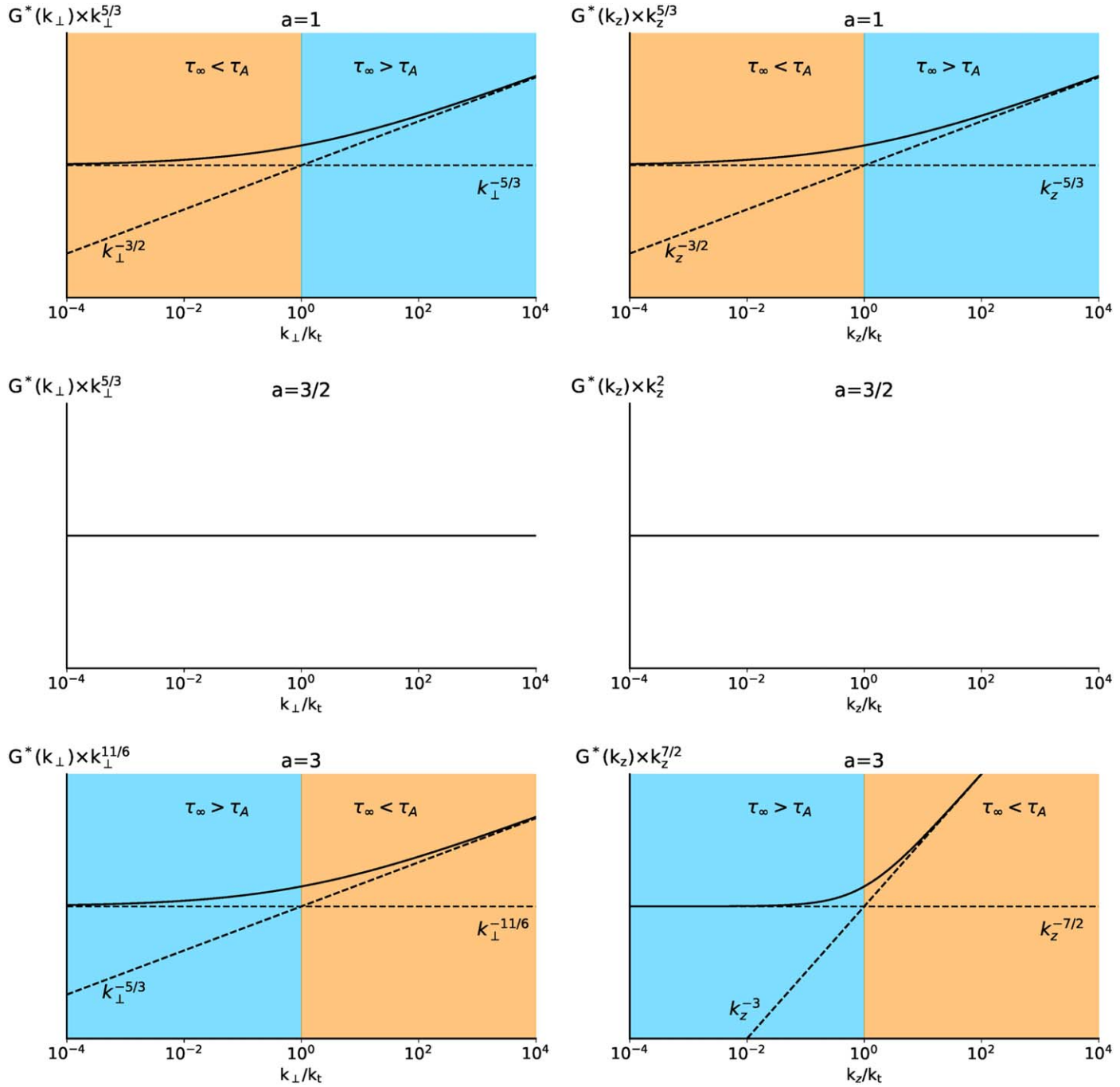

Figure 2. Top: plot of the predicted NI/slab inertial range compensated omnidirectional spectrum, showing that the spectrum transitions from a steeper Kolmogorov spectrum to a flatter IK spectrum at a transitional wavenumber $k_t^{-1} \equiv s^3 V_{A0}^3 (M_{A0}^I)^6 / (C_K^{3/2} \varepsilon_\infty)$. The orange region to the left of $k = k_t$ corresponds to $\tau_\infty < \tau_A$, and blue region to the right corresponds to $\tau_\infty > \tau_A$. For strongly imbalanced turbulence, the predicted spectrum is strictly Kolmogorov with $G^*(k) \sim k^{-5/3}$ when $a = 1$. The labeling of the dashed asymptotic lines refers to the uncompensated asymptotic wavenumber spectrum. Middle: plot of the NI/slab spectrum (46) when $a = 3/2$. Bottom: plot of the compensated NI/slab spectrum when $a = 3$. See text for details.

$$a = 3: \quad G^*(k_z) = C_* k_t^{4/3} k_z^{-3} \left(1 + \left(\frac{k_z}{k_t}\right)^{-1}\right)^{1/2}, \tag{58}$$

which yields

$$P_\parallel^{\rm total}(f) = P_\parallel^\infty(f) + P_\parallel^*(f), \tag{59}$$

where $q^\infty = 5/3$ and

$$P_\parallel^\infty(f) = \frac{2\pi}{U_0 \sin\Psi} \frac{3}{8} C_\infty \left(\frac{2\pi f}{U_0 \sin\Psi}\right)^{-5/3}; \tag{60}$$

$$a = 1: \quad P_\parallel^*(f) = \frac{2\pi}{U_0 \cos\Psi} \frac{1}{2} C_* \left(\frac{2\pi f}{U_0 \cos\Psi}\right)^{-5/3} \times \left(1 + \left(\frac{2\pi f}{U_0 \cos\Psi}\right)^{1/3} k_t^{-1/3}\right)^{1/2}; \tag{61}$$

$$a = 1, \tau_A \gg \tau_\infty: \quad P_\parallel^*(f) = \frac{2\pi}{U_0 \cos\Psi} \frac{1}{2} C_* \left(\frac{2\pi f}{U_0 \cos\Psi}\right)^{-5/3}; \tag{62}$$

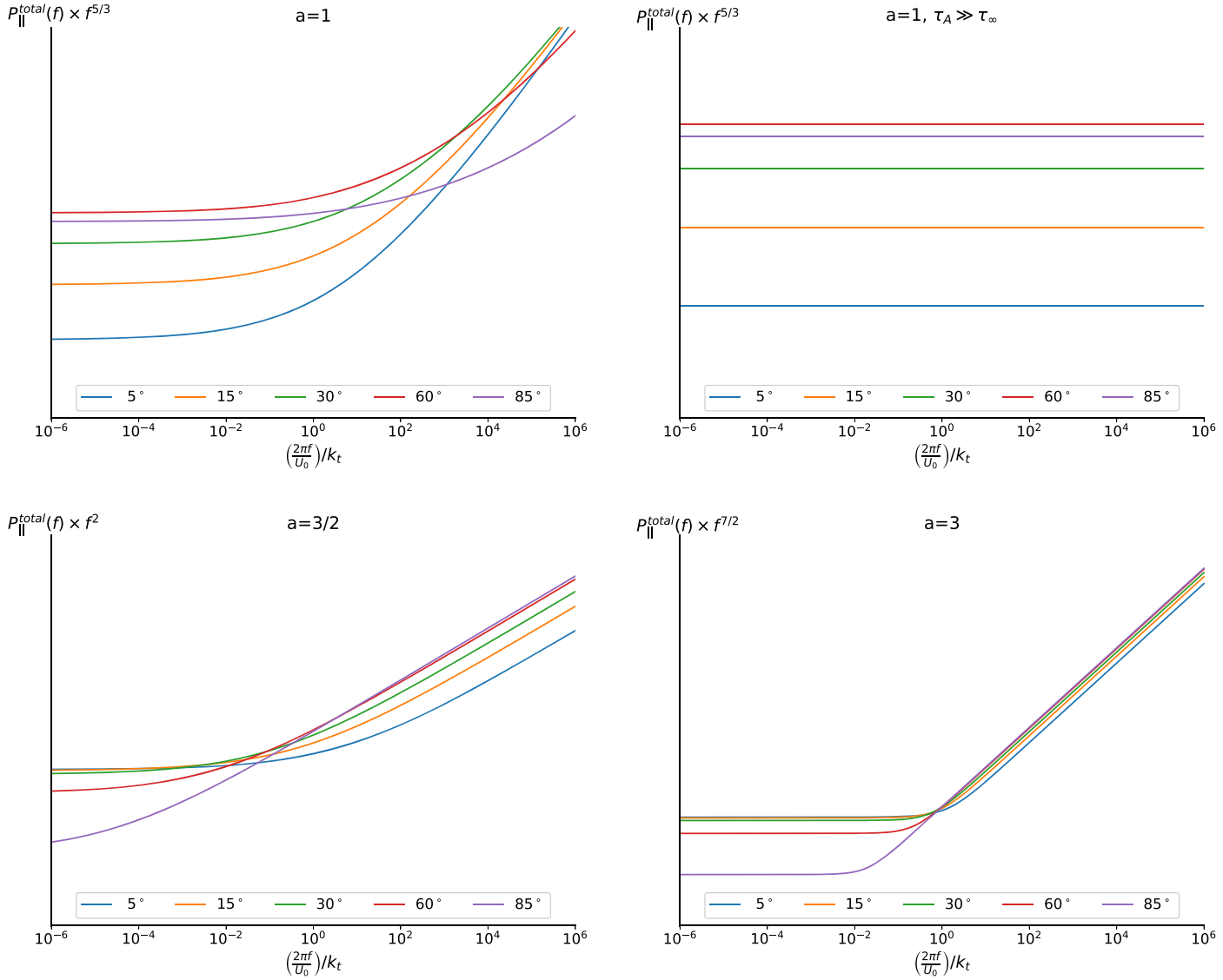

Figure 3. Compensated frequency power spectra for the total energy as expressed through the Elsässer variables for different choices of angle Ψ between the interplanetary magnetic field and the solar wind flow according to the 2D—NI/slab model (59)–(64). The angles range from highly aligned ($\Psi = 5°$) to highly oblique ($\Psi = 85°$). Top left: $a = 1$. Top right: $a = 1$ and $\tau_A \gg \tau_\infty$, i.e., highly imbalanced turbulence. Bottom left: $a = 3/2$. Bottom right: $a = 3$. See text for details.

$$a = \frac{3}{2}: \quad P_{\parallel}^{*}(f) = \frac{2\pi}{U_0 \cos\Psi}\frac{1}{2}C_{*}k_t^{1/3}\left(\frac{2\pi f}{U_0\cos\Psi}\right)^{-2}; \quad (63)$$

$$a = 3: \quad P_{\parallel}^{*}(f) = \frac{2\pi}{U_0 \cos\Psi}\frac{1}{2}C_{*}k_t^{4/3}\left(\frac{2\pi f}{U_0\cos\Psi}\right)^{-3} \times \left(1 + \left(\frac{2\pi f}{U_0\cos\Psi}\right)^{-1} k_t\right)^{1/2}. \quad (64)$$

Plotted in Figure 3 are compensated frequency power spectra for the total energy $\langle z^2\rangle = \langle z^{\infty 2}\rangle + \langle z^{*2}\rangle$ for different choices of angle Ψ between the interplanetary magnetic field and the solar wind flow. The top left panel of Figure 3 reflects the choice $a = 1$, and the top right panel corresponds to $a = 1$ and $\tau_A \gg \tau_\infty$. The bottom left panel shows the $a = 3/2$ case, and the bottom right panel shows the $a = 3$ case. Here $C_\infty = 0.8C_{\rm total}$, $C_* = 0.2C_{\rm total}$.

The top left panel of Figure 3, corresponding to $a = 1$, shows that for large values of Ψ the spectral slope of the frequency power spectrum remains close to $-5/3$ except for wavenumbers much greater than k_t, which exhibit IK scaling. For small angles Ψ ($\sim$15°, 5°), the frequency spectra are $f^{-5/3}$ for $(2\pi f/U_0)/k_t < 1$, but thereafter are $f^{-3/2}$. Most of the power is found at an angle $\Psi \simeq 60°$. The top right panel of Figure 3, corresponding to $a = 1$ and highly imbalanced turbulence $\tau_A \gg \tau_\infty$, shows that the spectra have a fixed spectrum $f^{-5/3}$ regardless of Ψ, with the only difference being that the most power is found when $\Psi \simeq 60°$. This example corresponds to the cases of highly imbalanced turbulence with a $-5/3$ frequency spectrum discussed in Telloni et al. (2019) and Zhao et al. (2020a) when $\Psi < 15°$. The bottom left panel of Figure 3, for $a = 3/2$, is quite different from the $a = 1$ plots. Only for low frequencies and angles $\Psi < 45°$ does the frequency spectrum satisfy f^{-2}; otherwise, the spectrum is close to $f^{-5/3}$. Most of the power is found in angles close to $\Psi \simeq 30°$ for this case. The bottom right panel of Figure 3, for $a = 3$, possesses a double-power-law structure, with low frequencies satisfying $f^{-7/2}$ and the higher frequencies being dominated by

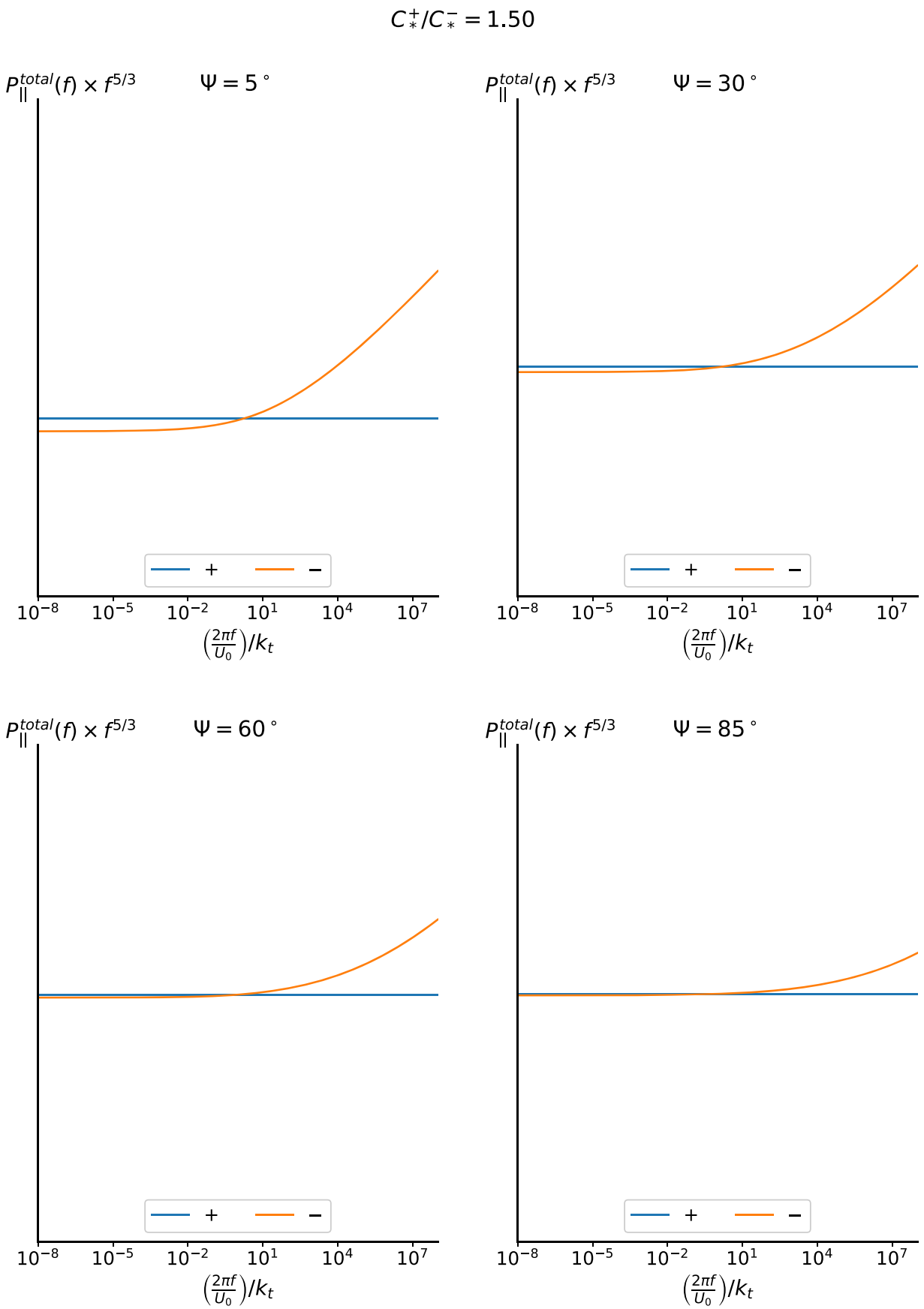

Figure 4. Compensated frequency power spectra for the total energy as expressed through the forward and backward Elsässer variables $\langle z^{*+2}\rangle$ and $\langle z^{*-2}\rangle$ for different choices of angle $\Psi = 5°$, 30°, 60°, and 85° between the interplanetary magnetic field and the solar wind flow according to the 2D—NI/slab model. $C_*^+/C_*^- = 1.5$. See text for details.

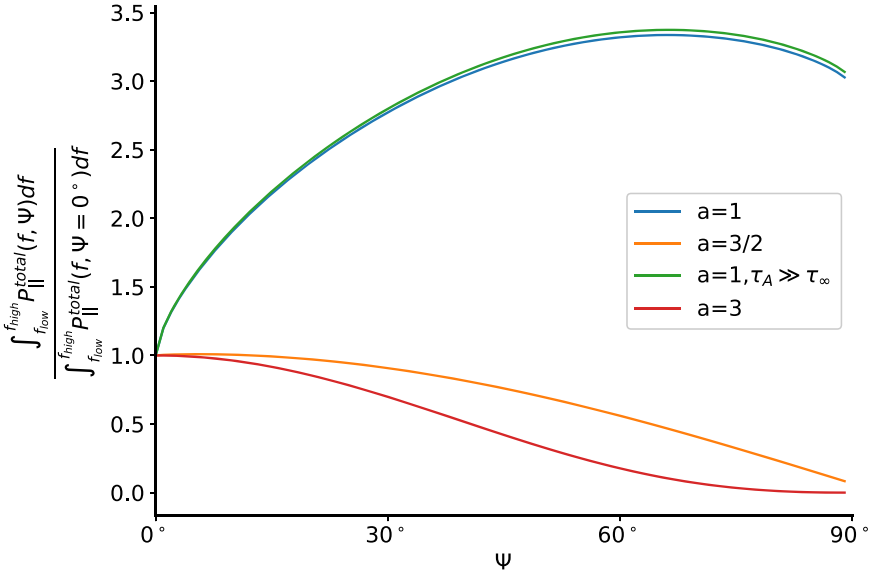

Figure 5. Integrated power measured parallel to the solar wind flow $\int_{f_{\rm low}}^{f_{\rm high}} P_{\parallel}^{\rm total}(f,\Psi)df$ as a function of angle Ψ between the interplanetary magnetic field and the solar wind flow. Here $f_{\rm low} = 2\pi U_0/\lambda_\perp^\infty$. For the four curves, the power is normalized by the value of the total power at $\Psi = 0°$.

the majority 2D component with an $f^{-5/3}$ spectrum because the NI/slab f^{-3} spectrum has very little power at high frequencies.

Figure 4 illustrates spectra for the forward and backward Elsässer energy densities $\langle z^{*+2}\rangle$ and $\langle z^{*-2}\rangle$ discussed above when $a = 1$ and $\tau_3^+ \neq \tau_3^-$, $\tau_A \gg \tau_\infty$ for $\langle z^{*+2}\rangle$ and τ_A and τ_∞ finite for $\langle z^{*-2}\rangle$. For this case, we have

$$P_{\parallel}^{\rm total\pm}(f) = P_{\parallel}^{\infty}(f) + P_{\parallel}^{*\pm}(f), \tag{65}$$

where $P_{\parallel}^{\infty}(f)$ is given by Equation (60) and

$$P_{\parallel}^{-*}(f) = \frac{2\pi}{U_0\cos\Psi}\frac{1}{2}C_*^-\left(\frac{2\pi f}{U_0\cos\Psi}\right)^{-5/3} \times\left(1+\left(\frac{2\pi f}{U_0\cos\Psi}\right)^{1/3}k_t^{-1/3}\right)^{1/2}; \tag{66}$$

$$P_{\parallel}^{*+}(f) = \frac{2\pi}{U_0\cos\Psi}\frac{1}{2}C_*^+\left(\frac{2\pi f}{U_0\cos\Psi}\right)^{-5/3}. \tag{67}$$

Note that $C_* = C_*^+ + C_*^-$ to preserve the ratio between the 2D and NI/slab components. Figure 4 shows four angles for $\Psi = 5°$, $30°$, $60°$, and $85°$, with an assumed ratio of $C_*^+/C_*^- = 1.5$. The distinction between the forward and backward spectra is most pronounced for small values of Ψ, although the flattening of the $\langle z^{*-2}\rangle$ power spectrum persists for all ***U–B*** angles, offering an intriguing explanation for a similar flattening seen sometimes in Helios data (Tu et al. 1989, 1990; Marsch & Tu 1990).

Figure 5 is a plot of the integrated power measured parallel to the solar wind flow as a function of angle Ψ, i.e., $\int_{f_{\rm low}}^{f_{\rm high}} P_{\parallel}^{\rm total}(f,\Psi)df$ for each of the four cases illustrated in Figure 3. Each curve is normalized to its total power at $\Psi = 0°$. For $a = 1$ and both τ_A finite or infinite, the largest measured power is found when $\Psi \simeq 65°$ since this angle maximizes the NI/slab contribution in the 2D + NI/slab superposition model. By contrast, the power for the $a = 3/2$ case decreases monotonically and without inflection as Ψ increases from 0° to 90°, primarily because the spectrum at low frequencies is dominated by NI/slab fluctuations with an f^{-2} spectrum even though the 2D fluctuations are energetically dominant. The $a = 3$ curve is similar in that the integrated power parallel to the solar wind flow decreases monotonically with increasing Ψ but has an inflection point as Ψ approaches 90°.

4. Conclusions and Discussion

The foundation of the popular 2D + slab superposition solar wind turbulence model is NI MHD in the plasma beta $\sim$1 or $\ll$1 regimes. Based on the equations describing NI MHD in this regime, we provide a detailed spectral analysis appropriate to 2D + NI/slab turbulence. In part this analysis was motivated by a series of studies (Matthaeus et al. 1990; Bieber et al. 1996; Saur & Bieber 1999; Dasso et al. 2005; Horbury et al. 2008, 2012; Podesta 2009; Wicks et al. 2010; Forman et al. 2011; Wang et al. 2015; Telloni et al. 2019; Wu et al. 2020; Zhao et al. 2020a) investigating the underlying anisotropy of low-frequency MHD turbulence and the possibility that the 2D + NI/slab model may be important to coronal turbulence and the associated heating problem (Zank et al. 2018a; Adhikari et al. 2020b; Zhao et al. 2020b). Unlike the standard 2D + slab model, in which spectral power resides only in the 2D plane perpendicular to and along the $\hat{z}$-axis parallel to the mean magnetic field $\boldsymbol{B}_0$, the NI MHD-based 2D + NI/slab model has wave power throughout the wavenumber plane.

Our principle results can be summarized as follows.

1. The ordering underlying the NI MHD expansion in the plasma $\beta \sim 1$ or $\ll$1 regime implies that the ratio of the magnetic energy density in 2D to slab fluctuations is roughly 80:20, i.e., the 2D (in the plane orthogonal to the mean magnetic field $\boldsymbol{B}_0$) component is the dominant or majority component and the slab component is the minority turbulence component.
2. The majority 2D component possesses the classical Kolmogorov spectrum $G^\infty(k_\perp) \sim k_\perp^{-5/3}$ in the perpendicular wavenumber $k_\perp$.

3. NI MHD shows that the NI/slab component is coupled in a passive sense to the dominant 2D fluctuations. The incompressible NI component comprises both Alfvénic and higher-order quasi-2D fluctuations (the latter are not strictly 2D, unlike the majority component). The passive coupling of 2D and NI fluctuations ensures that the 2D nonlinear timescale is important in determining the triple-correlation timescale for the minority NI turbulence component.
4. In the NI limit in which all the energy resides in a single NI component (e.g., $\langle z^{*+2}\rangle \neq 0$ and $\langle z^{*-2}\rangle = 0$), the NI spectrum is given by $G^*(k_z) \sim k_z^{-5/3}$ and $G^*(k_\perp) \sim k_\perp^{-5/3}$ for $k_z = k_\perp$. For solar wind flows that are highly aligned with the mean magnetic field, this result corresponds to observing approximately unidirectional Alfvén wave propagation and a $k_\parallel^{-5/3}$ spectrum, where $k_\parallel$ is the wavenumber parallel to the mean flow. The physical interpretation of this result is that nonlinear interactions are not the result of counterpropagating Alfvén waves but instead unidirectionally propagating Alfvén waves responding in a passive sense to the majority 2D turbulence. Such observations in the solar wind are interpreted typically as "Alfvénic solar wind turbulence" despite the inability of unidirectional Alfvén wave propagation to support turbulence and the associated dissipative heating needed to produce a nonadiabatic solar wind temperature profile. Instead, our results indicate that the fast and slow solar wind is dominated by quasi-2D turbulence that in the case of highly magnetic-field-aligned flows cannot be measured by a single spacecraft. However, the Alfvénic and/or slab component of the 2D + NI/slab decomposition of NI MHD can be measured directly by a single spacecraft, which then leads to an interpretation as "Alfvénic turbulence." Adhikari et al. (2020a) present a coupled solar wind—coronal plasma and turbulence transport model that incorporates the evolution and dissipation of quasi-2D turbulence and unidirectionally propagating Alfvén waves. The model appears to be consistent with observations of the fast solar wind made by the PSP mission.
5. The inverse triple-correlation time that determines in part spectral transfer for the NI component is to leading order the sum of the inverse majority 2D nonlinear timescale τ_∞ and a generalized form of the inverse Alfvén timescale $\tau_A^{-1} = (V_{A0}/\lambda_A)(1-\sigma_c^{*2})^{1/2} {M_{A0}^t}^2$. The new form of the Alfvén timescale captures the properties that (1) $\tau_A^{-1} = 0$ if $|\sigma_c^*| = 1$, ensuring that no spectral transfer can occur for unidirectional Alfvén wave propagation (unless mediated by the "passive" response to 2D turbulence), and (2) balanced turbulence yields $\tau_A^{-1} = (V_{A0}/\lambda_A)(M_{A0}^t)^2$ since $|\sigma_c^*| = 0$.
6. Use of a Kolmogorov phenomenology shows that the spectrum is governed by the ratio of the nonlinear and Alfvén timescales, with distinctly different spectra corresponding to either strong turbulence, when the turbulence is dominated by quasi-2D interactions ($\tau_A \gg \tau_\infty$), or weak turbulence, which is dominated by propagation effects associated with Alfvén waves ($\tau_\infty \gg \tau_A$). The strong and weak turbulence regimes are separated in k by a transition wavenumber ${k_t}^{-1} \equiv s^3 (M_{A0}^t)^6/(M_{A0}^\infty)^3 \lambda_\perp^\infty$ that exceeds the wavenumber associated with the 2D correlation length. Depending on parameters, k_t may lie in the observed inertial length, in which case we would expect the Elsässer energy spectral slope to undergo a change in slope. The transition wavenumber k_t is a measure of the strength of the turbulence and hence whether nonlinear or wave effects dominate the cascade.
7. The observed anisotropy of the wavenumber correlation function suggests that there is a nonlinear relation between $k_\perp$and k_z. We introduce one possible relation between wavenumbers perpendicular to and aligned with the mean magnetic field, $k_\perp \sim k_z^a$, $a > 0$. Here the anisotropy parameter a may be regarded as a measure of wavenumber anisotropy, and $a = 1$ corresponds to isotropy. Based on this relation, general forms of the 1D spectra along and perpendicular to $\boldsymbol{B}_0$, $G^*(k_z)$ (Equation (42)) and $G^*(k_\perp)$ (Equation (45)), respectively, can be derived for the NI/slab component. Regardless of the choice of a, $G^*(k_\perp) \sim k_\perp^{-5/3}$ for strong turbulence always.
8. For a choice of $a = 1$, i.e., $k_\perp = k_z$ (i.e., wavenumber isotropy), and finite τ_∞ and τ_A, the 1D inertial range spectrum for strong NI/slab turbulence is Kolmogorov with $G^*(k) \sim k^{-5/3}$, whereas that for weak NI/slab turbulence is the IK spectrum $G^*(k) \sim k^{-3/2}$. The transition from strong/Kolmogorov ($\tau_A > \tau_\infty$) to weak/IK ($\tau_\infty > \tau_A$) turbulence occurs at the transition wavenumber k_t, provided that it lies in the inertial range, illustrating that the wavenumber spectrum can flatten for $k > k_t$.
9. The choice of $a = 3/2$ corresponds to balanced timescales $\tau_A = \tau_\infty$, or equivalently that the ratio τ_∞/τ_A is independent of wavenumber, i.e., critical balance. In this case, the NI/slab spectra are given by $G^*(k_z) \sim k_z^{-2}$ and $G^*(k_\perp) \sim k_\perp^{-5/3}$.
10. The choice of $a < 3/2$ implies that $\tau_A > \tau_\infty$ for all $k < k_t$ (i.e., strong turbulence) and $\tau_\infty > \tau_A$ for all $k > k_t$ (i.e., weak turbulence), and that the spectrum flattens in transitioning from the strong to weak turbulence regime. Such a transition is obviously absent when $a = 3/2$ because τ_∞/τ_A is independent of wavenumber. The choice of $a > 3/2$ implies that $\tau_\infty > \tau_A$ for all $k < k_t$ (wave-dominated or weak turbulence regime) and $\tau_A > \tau_\infty$ for all $k > k_t$ (i.e., strong turbulence and dominated by nonlinear interactions). For the latter case, the transition from a steep to a flatter spectrum corresponds now to a transition from weak to strong NI/slab turbulence.
11. For strongly imbalanced turbulence, $G^*(k_\perp) \sim k_\perp^{-5/3}$ always and for $a = 1$, $G^*(k_z) \sim k_z^{-5/3}$.
12. The NI spectral analysis was extended to include the forward and backward Elsässer variables $\boldsymbol{z}^{*\pm}$ with corresponding triple-correlation timescales $\tau_3^\pm$. In the case that $\tau_3^+ = \tau_3^-$, we recover the same spectral results found for $\langle z^{*2}\rangle = \langle z^{*+2}\rangle + \langle z^{*-2}\rangle$, i.e., $G^{*\pm}(k_z)$ and $G^{*\pm}(k_\perp)$ are given by Equations (42) and (45), respectively, and the G^{*+} and the G^{*-} spectra are the same. However, if $\tau_3^+ \neq \tau_3^-$, the spectra for G^{*+} and G^{*-} are different. For example, if $\tau_A \gg \tau_\infty$ for the forward Elsässer component $\boldsymbol{z}^{*+}$ and both τ_A and τ_∞ are finite for the backward component $\boldsymbol{z}^{*-}$, then $G^{*+}(k) \sim k^{-5/3}$ and $G^{*-}(k) \sim k^{-5/3}$ for $k < k_t$ and $\sim k^{-3/2}$ for $k > k_t$, i.e., the forward and backward Elsässer variable spectra differ in that one is Kolmogorov and the other has a double-power-law form, flattening from $-5/3$ to $-3/2$ in

spectral index. Tu et al. (1989, 1990) and Marsch & Tu (1990) report observations of Elsässer spectra that resemble such a predicted form.

13. By computing the total spectrum in frequency parallel to the solar wind flow for the 2D + NI/slab model, i.e., $P_{\parallel}^{\rm total}(f) = P_{\parallel}^{\infty}(f) + P_{\parallel}^{*}(f)$, we can predict the frequency spectrum that a spacecraft would observe as a function of the angle Ψ between the mean flow vector $\boldsymbol{U}$ and magnetic field $\boldsymbol{B}_0$. For finite τ_∞ and τ_A and $a = 1$, $P_{\parallel}^{\rm total}(f) \sim f^{-5/3}$ for all $k \leqslant k_t$ and all possible angles Ψ. For $k > k_t$, the spectrum flattens with $P_{\parallel}^{\rm total}(f) \sim f^{-3/2}$. For strong turbulence ($\tau_A \gg \tau_\infty$) and $a = 1$, $P_{\parallel}^{\rm total}(f) \sim f^{-5/3}$ for all k and all Ψ. By contrast, setting $a = 3/2$ yields $P_{\parallel}^{\rm total}(f) \sim f^{-2}$ for low frequencies and angles $\Psi < 45°$; otherwise, the spectrum is close to $f^{-5/3}$ because the 2D component begins to dominate the spectrum. Finally, we note that for values $a > 3/2$, such as $a = 3$, a double-power-law structure is possible for $P_{\parallel}^{\rm total}(f)$, with higher frequencies having a spectrum $f^{-5/3}$ because the 2D component dominates.
14. An important point is that the frequency spectrum for highly aligned flows will be determined by the slab component predominantly rather than by quasi-2D fluctuations. Since the slab fluctuations are Alfvénic, they will not be intermittent, whereas more oblique flows, being increasingly dominated by quasi-2D turbulence and structures, will exhibit higher levels of intermittency.
15. In the case that $\tau_3^+ \neq \tau_3^-$, distinctly different spectra for $P_{\parallel}^{\rm total}(f)$ are most easily observed when Ψ is small.
16. Finally, we find that the integrated power measured parallel to the solar wind flow as a function of Ψ possesses very different characteristics depending on whether $a < 3/2$, $a = 3/2$, or $a > 3/2$. For $a < 3/2$ ($a = 1$), the power increases from $\Psi = 0°$ until it peaks at about $\Psi = 65°$, after which it decreases modestly until $\Psi = 90°$. By contrast, the power for the critical balance case $a = 3/2$ decreases without inflection from $\Psi = 0°$ to 90°. In the case of $a > 3/2$ ($a = 3$), the power decrease is similar to the $a = 3/2$ case, although somewhat faster before flattening for values $\Psi \geqslant 60°$.

In summary, based on the theory of NI MHD, we have provided a complete analysis of the spectral characteristics of the majority 2D + minority NI/slab superposition model. The analysis provides a framework within which observations of solar wind turbulence in the inertial range can be interpreted. It is of some interest that the anisotropies associated with critical balance emerge from the NI MHD description in the plasma beta regime $\beta \sim 1$ and $\ll 1$.

We acknowledge the partial support of an NSF EPSCoR RII-Track-1 Cooperative Agreement OIA-1655280 and partial support from an NSF/DOE Partnership in Basic Plasma Science and Engineering via NSF grant PHY-1707247 and a NASA Parker Solar Probe contract SV4-84017. D.T. was partially supported by the Italian Space Agency (ASI) under contract I/013/12/0.

ORCID iDs

G. P. Zank https://orcid.org/0000-0002-4642-6192
M. Nakanotani https://orcid.org/0000-0002-7203-0730
L.-L. Zhao https://orcid.org/0000-0002-4299-0490
L. Adhikari https://orcid.org/0000-0003-1549-5256
D. Telloni https://orcid.org/0000-0002-6710-8142

References

Adhikari, L., Zank, G., & Zhao, L.-L. 2020a, ApJ, in press
Adhikari, L., Zank, G. P., Hunana, P., et al. 2017a, ApJ, 841, 85
Adhikari, L., Zank, G. P., Telloni, D., et al. 2017b, ApJ, 851, 117
Adhikari, L., Zank, G. P., Zhao, L. L., et al. 2020b, ApJS, 246, 38
Bhattacharjee, A., Ng, C. S., & Spangler, S. R. 1998, ApJ, 494, 409
Bieber, J. W., Wanner, W., & Matthaeus, W. H. 1996, JGR, 101, 2511
Dasso, S., Milano, L. J., Matthaeus, W. H., & Smith, C. W. 2005, ApJL, 635, L181
Dobrowolny, M., Mangeney, A., & Veltri, P. 1980a, A&A, 83, 26
Dobrowolny, M., Mangeney, A., & Veltri, P. 1980b, PhRvL, 45, 144
Forman, M. A., Wicks, R. T., & Horbury, T. S. 2011, ApJ, 733, 76
Goldreich, P., & Sridhar, S. 1995, ApJ, 438, 763
Goldreich, P., & Sridhar, S. 1997, ApJ, 485, 680
Grappin, R., Frisch, U., Pouquet, A., & Leorat, J. 1982, A&A, 105, 6
Grappin, R., Leorat, J., & Pouquet, A. 1983, A&A, 126, 51
Horbury, T. S., Forman, M., & Oughton, S. 2008, PhRvL, 101, 175005
Horbury, T. S., Wicks, R. T., & Chen, C. H. K. 2012, SSRv, 172, 325
Huang, N. E., Shen, Z., Long, S. R., et al. 1998, RSPSA, 454, 903
Hunana, P., & Zank, G. P. 2010, ApJ, 718, 148
Klainerman, S., & Majda, A. 1982, CPAM, 35, 629
Marsch, E. 1991, in Reviews of Modern Astronomy, Vol. 4, ed. G. Klare (Berlin: Springer), 145
Marsch, E., & Tu, C. Y. 1990, JGR, 95, 8211
Matthaeus, W. H., & Brown, M. R. 1988, PhFl, 31, 3634
Matthaeus, W. H., Goldstein, M. L., & Roberts, D. A. 1990, JGR, 95, 20673
Matthaeus, W. H., Oughton, S., Pontius, D. H., Jr., & Zhou, Y. 1994, JGR, 99, 19267
Matthaeus, W. H., & Smith, C. 1981, PhRvA, 24, 2135
Matthaeus, W. H., & Zhou, Y. 1989, PhFlB, 1, 1929
Montgomery, D., Brown, M. R., & Matthaeus, W. H. 1987, JGR, 92, 282
Oughton, S., & Matthaeus, W. H. 2020, ApJ, 897, 37
Podesta, J. J. 2009, ApJ, 698, 986
Pouquet, A., Frisch, U., & Leorat, J. 1976, JFM, 77, 321
Ruiz, M. E., Dasso, S., Matthaeus, W. H., Marsch, E., & Weygand, J. M. 2011, JGRA, 116, A10102
Saur, J., & Bieber, J. W. 1999, JGR, 104, 9975
Telloni, D., Carbone, F., Bruno, R., et al. 2019, ApJ, 887, 160
Tu, C. Y., Marsch, E., & Rosenbauer, H. 1990, GeoRL, 17, 283
Tu, C. Y., Marsch, E., & Thieme, K. M. 1989, JGR, 94, 11739
von Karman, T., & Howarth, L. 1938, RSPSA, 164, 192
Wang, X., Tu, C., He, J., et al. 2015, ApJL, 810, L21
Weygand, J. M., Matthaeus, W. H., Dasso, S., et al. 2009, JGRA, 114, A07213
Wicks, R. T., Horbury, T. S., Chen, C. H. K., & Schekochihin, A. A. 2010, MNRAS, 407, L31
Wu, H., Tu, C., Wang, X., et al. 2020, ApJ, 892, 138
Zank, G. P. 2014, Transport Processes in Space Physics and Astrophysics, Lecture Notes in Physics, Vol. 877 (Berlin: Springer)
Zank, G. P., Adhikari, L., Hunana, P., et al. 2017, ApJ, 835, 147
Zank, G. P., Adhikari, L., Hunana, P., et al. 2018a, ApJ, 854, 32
Zank, G. P., Adhikari, L., Zhao, L. L., et al. 2018b, ApJ, 869, 23
Zank, G. P., Dosch, A., Hunana, P., et al. 2012, ApJ, 745, 35
Zank, G. P., & Matthaeus, W. H. 1992, JGR, 97, 17189
Zank, G. P., & Matthaeus, W. H. 1993, PhFl, 5, 257
Zank, G. P., Matthaeus, W. H., & Smith, C. W. 1996, JGR, 101, 17093
Zank, G. P., Nakanotani, M., & Webb, G. M. 2019, ApJ, 887, 116
Zhao, L. L., Adhikari, L., Zank, G. P., Hu, Q., & Feng, X. S. 2017, ApJ, 849, 88
Zhao, L.-L., Zank, G., Adhikari, L., et al. 2020a, ApJ, 898, 113
Zhao, L. L., Zank, G. P., Adhikari, L., et al. 2020b, ApJS, 246, 26
Zhao, L. L., Zank, G. P., Khabarova, O., et al. 2018, ApJL, 864, L34
Zhou, Y., & Matthaeus, W. H. 1990, JGR, 95, 14863
Zhou, Y., Matthaeus, W. H., & Dmitruk, P. 2004, RvMP, 76, 1015